

# TanDEM-X Pol-InSAR Performance for Forest Height Estimation

Florian Kugler, Daniel Schulze, Irena Hajnsek, *Fellow, IEEE*, Hans Pretzsch, and Konstantinos P. Papathanassiou, *Fellow, IEEE*

**Abstract**—TanDEM-X and TerraSAR-X platforms form together the first spaceborne single-pass polarimetric interferometer in space. This allows, for the first time, the acquisition of spaceborne polarimetric synthetic aperture radar interferometry (Pol-InSAR) data without the disturbing effect of temporal decorrelation. This paper aims to assess the potential of such data for forest applications. For this, single- and dual-pol data acquired over a boreal, a temperate, and a tropical site were investigated to characterize X-band penetration and polarization diversity of the interferometric coherence measurements. Pol-InSAR forest height inversion schemes have been proposed and implemented for the single- and dual-pol cases and cross validated against LIDAR reference measurements for all sites. The single-pol inversion relies on an external ground digital terrain model (DTM) and performed well for all sites with correlation coefficients  $r^2$  between 0.80 and 0.98. The dual-pol inversion does not require an external DTM but depends on the visibility of the whole forest layer. Accordingly, its performance varied with forest structure and season: The best performance was achieved for the summer acquisition of the boreal test site ( $r^2 = 0.86$ ) and for the winter acquisition of the temperate test site ( $r^2 = 0.77$ ). For the tropical test site, only a weak correlation ( $r^2 = \sim 0.50$ ) could be established.

**Index Terms**—Forest, forest height, forest parameter, interferometry, polarimetric synthetic aperture radar interferometry (Pol-InSAR), synthetic aperture radar (SAR), TanDEM-X, TerraSAR-X, X-band.

## I. INTRODUCTION

**P**OLARIMETRIC synthetic aperture radar interferometry (Pol-InSAR) has been demonstrated to be a powerful radar remote sensing technique for the quantitative estimation of forest structure parameters [1]. The interferometric coherence is directly related to the vertical distribution of scatterers. In consequence, the coherent combination of single- or multi-baseline interferograms at different polarizations allows the

characterization of the vertical scattering structure of a volume scatterer [1], [3], [4]. Indeed, forest height and structure parameter estimation from polarimetric single- and multibaseline data acquired at lower frequencies (L- and P-bands) have been successfully demonstrated in a series of airborne experiments in natural, as well as commercial, boreal, temperate, and tropical test sites for different stand and terrain conditions [3], [5]–[8].

However, when it comes to spaceborne repeat pass implementations, the inherent presence of temporal decorrelation biases the interferometric coherence estimates, thus degrading the sensitivity to vertical scattering structure and limiting the performance of Pol-InSAR inversion techniques [5], [9]–[11]. Short-term decorrelation effects (for example, wind-induced temporal decorrelation) affect Pol-InSAR acquisitions even at short temporal baselines on the order of a few hours up to a few days [5], [10]. This is the main reason why polarimetric spaceborne missions such as Canadian Space Agency's RadarSAT-2 (C-band) or the Japanese Aerospace Exploration Agency's ALOS-PalSAR (L-band) could not essentially contribute neither to a large-scale demonstration of Pol-InSAR techniques nor to the development of new Pol-InSAR applications [10], [11].

The TanDEM-X (TDX, launched in June 2010) and TerraSAR-X (TSX, launched in June 2007) platforms together form the first single-pass polarimetric interferometer in space and allow, for the first time, the acquisition of single-, dual-, and quad-polarimetric Pol-InSAR data without the disturbing effect of temporal decorrelation. Unfortunately, the fact that vegetation extinction increases with frequency, reducing the penetration into (and through) vegetation layers, makes X-band a rather suboptimal choice for forest structure mapping, at least in a global sense.

However, a number of InSAR experiments have indicated that, in several cases—primarily in boreal and less dense forest environments—a rather surprising penetration into forest and vegetation scatterers occurs [5]–[7], [12], [13]. This has been supported by interferometric and radargrammetric analyses of spaceborne repeat pass data from TSX and COSMO-SkyMed [14].

Pol-InSAR forest height inversion at X-band was first demonstrated in the boreal zone on the basis of a single-polarization interferometric acquisition and by fixing the extinction [7]. In [8], forest height inversion was performed using dual-pol (HH and HV) interferometric acquisitions over a number of pine stands in France. More recent experiments have demonstrated the sensitivity of X-band interferometric measurements on forest vertical structure attributes in temperate

Manuscript received June 9, 2013; revised November 2, 2013; accepted November 11, 2013.

F. Kugler, D. Schulze, and K. P. Papathanassiou are with the Microwaves and Radar Institute, German Aerospace Center (DLR-HR), 82234 Oberpfaffenhofen, Germany (e-mail: florian.kugler@dlr.de; daniel.schulze@dlr.de; kostas.papathanassiou@dlr.de).

I. Hajnsek is with the Institut für Umweltingenieurwissenschaften, Swiss Federal Institute of Technology (ETH) Zürich, 8093 Zürich, Switzerland and also with the Microwaves and Radar Institute, German Aerospace Center (DLR-HR), 82234 Oberpfaffenhofen, Germany (e-mail: hajnsek@ifu.baug.ethz.ch; irena.hajnsek@dlr.de).

H. Pretzsch is with the Chair for Forest Growth and Yield Science, Department for Ecosystem and Landscape Management, Center of Life and Food Sciences, Technische Universität München, 85354 Freising, Germany (e-mail: hans.pretzsch@lrz.tum.de).

Color versions of one or more of the figures in this paper are available online at <http://ieeexplore.ieee.org>.

Digital Object Identifier 10.1109/TGRS.2013.2296533

forests [12], [16], [17]. In tropical forests, one of the first interferometric scattering models describing penetration and backscattering at X-band was developed in [18] and [19] and was used to interpret the observed coherence loss on emergent trees in tropical rain forests. Finally, in [5], forest height estimation over a tropical peat swamp forest was demonstrated using a single-polarization interferometric acquisition and a LIDAR-derived ground digital terrain model (DTM). These results have triggered the interest to explore the potential and the limitations of Pol-InSAR applications at X-band. TDX provides the unique opportunity to systematically investigate Pol-InSAR data over a wide range of forest sites under different seasonal and environmental conditions in order to improve the understanding of vegetation scattering processes at X-band and to assess the potential of Pol-InSAR techniques at this frequency band.

For this investigation, a number of single- and dual-pol data acquired by TDX at different operation modes (briefly described in Section II) and geometries over a number of forests in different ecosystems have been evaluated. Three different forest types representative for different forest ecosystems at different seasons were investigated: a boreal forest (Krycklan,  $64^{\circ}10'$  north and  $20^{\circ}01'$  east), a temperate forest (Traunstein,  $47^{\circ}52'$  north,  $12^{\circ}39'$  east), and a tropical forest (Mawas,  $-2^{\circ}09'$  south and  $114^{\circ}27'$  east). The test sites, the data sets, and the calculation of the reference height, i.e., forest top height H100, from LIDAR data are described in Section III. In order to draw conclusions about the potential of TanDEM-X to derive forest height by means of Pol-InSAR techniques, three important questions need to be answered: The first one is the question about the penetration of X-band into different forest types and forest conditions. The second one is the question about the role of polarimetry, i.e., about the degree of polarimetric diversity of the interferometric measurements. Finally, the third one is the question about how accurate (and how robust) forest height can be estimated exploring the information content of the polarimetric interferometric measurements. In Section IV, the penetration of X-band into the forest volume and the polarimetric diversity of the interferometric coherence measurements are investigated. To accomplish this, the height of the scattering center and the maximized polarimetric phase difference were cross validated against forest top height H100 (estimated from LIDAR data). In addition, here, seasonal differences in the scattering behavior are discussed. In Section V, a single- and a dual-pol Pol-InSAR inversion scheme are introduced. Forest height inversion results for each test site and both inversion scenarios are cross validated against LIDAR-derived reference measurements in Section VI. Finally, the achieved results are summarized and discussed in Section VII.

## II. TANDEM-X INTERFEROMETRIC PARAMETERS

### A. Interferometric Modes

TDX can operate in different interferometric configurations, of which the most common are [20], [21] the following.

- 1) The pursuit monostatic mode, where the two satellites (TDX and TSX) are independently operated and separated by an along-track distance that induces a temporal

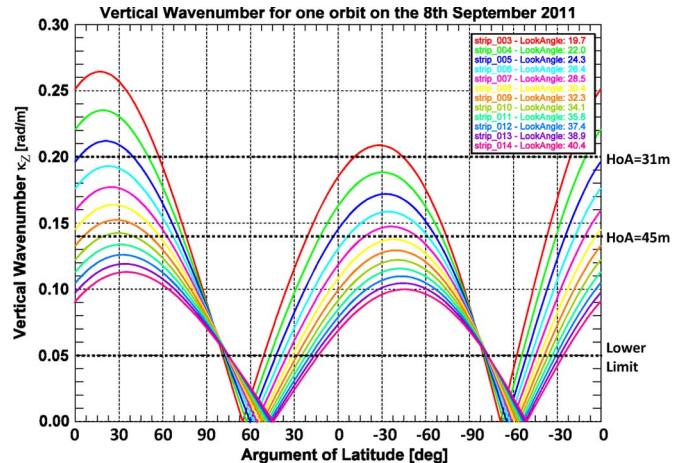


Fig. 1. Vertical wavenumber  $\kappa_Z$  as a function of orbit position (latitude) for one orbit cycle ( $360^{\circ}$ ) starting from the equator ( $0^{\circ}$ ) in ascending orbit pass for the 12 full-performance TDX beams in stripmap mode (beam “strip\_003” to beam “strip\_014”). Each beam is associated with a certain look angle.

baseline. This configuration was used in the monostatic commissioning phase of TDX with an along-track separation on the order of 20 km that translated to a temporal baseline of approximately 3 s.

- 2) The bistatic mode, where one of the two satellites (either TDX or TSX) acts as a transmitter and both satellites receive the scattered signal simultaneously, reducing the temporal baseline to practically zero.
- 3) The alternating bistatic mode, where, similar to the conventional bistatic mode, one satellite is transmitting and both satellites simultaneously receive. However, in this mode, the transmitter role is alternated between the two satellites on a pulse-by-pulse basis. Accordingly, the images acquired in the alternating bistatic mode allow the formation of one interferogram corresponding to the monostatic, i.e., to the “both antennas transmit—both antennas receive” configuration, and one corresponding to the bistatic, i.e., the “one antenna transmits—both antennas receive” configuration, at the same time. The second interferogram has half effective baseline of the first [20].

All three interferometric modes can be realized in stripmap, ScanSAR, spotlight, and sliding spotlight imaging modes operated in a single- or a dual-polarimetric mode with look angles ranging between  $15^{\circ}$  and  $55^{\circ}$  ( $20^{\circ}$  and  $41^{\circ}$  for the 12 dedicated full-performance stripmap beams) [22].

### B. Effective Spatial Baseline

The performance of quantitative polarimetric interferometric techniques critically depends on the effective spatial baseline used for the interferometric acquisition(s). The parameter commonly used to express the effective spatial baseline is the vertical wavenumber  $\kappa_Z$  approximated by

$$\kappa_Z = m \frac{2\pi\Delta\theta}{\lambda \sin(\theta)} \approx m \frac{2\pi B_{\perp}}{\lambda \sin(\theta)R} \quad (1)$$

where  $\Delta\theta$  is the angular separation of the two acquisitions in the direction of the resolution cell,  $B_{\perp}$  is the effective

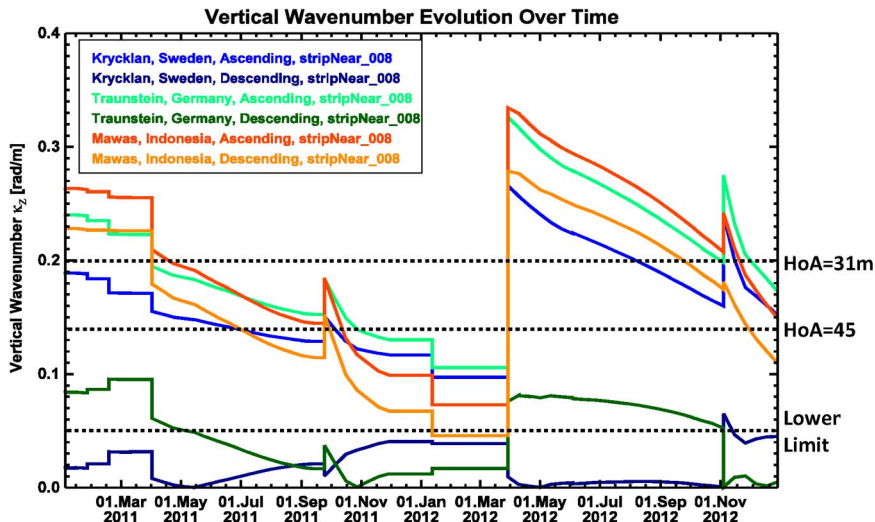


Fig. 2. Development of the vertical wavenumber  $\kappa_Z$  as a function of mission time for beam strip\_008 (look angle =  $\sim 30.4^\circ$ ) for the three test sites Krycklan (latitude:  $64^\circ 10'$ ), Traunstein (latitude:  $47^\circ 52'$ ), and Mawas (latitude:  $-2^\circ 19'$ ) in ascending and descending orbit pass.

(perpendicular) baseline,  $\theta$  is the local incidence angle,  $\lambda$  is the used wavelength,  $R$  is the slant range distance, and  $m$  accounts for the acquisition mode. For monostatic acquisitions,  $m = 2$ , whereas for bistatic acquisitions,  $m = 1$ . The vertical wavenumber  $\kappa_Z$  scales the interferometric phase to height. In the case of TanDEM-X, the parameter used to express the effective spatial baseline is the height of ambiguity  $\text{HoA} = 2\pi/\kappa_Z$ , i.e., the height that corresponds to an interferometric phase change of  $2\pi$ .

The TanDEM-X mission scenario and orbit parameters are designed to fulfill the specification of the digital elevation model (DEM) product. To accomplish this, the Earth's total landmass will be mapped at least twice, in two acquisition periods, with heights of ambiguity ranging from 35 to 60 m. Global DEM data acquisition with varying baselines will continue until 2014 [23].

During the mission time, the two satellites (TSX and TDX) are flying in a close helix formation (for a detailed description, see [20], [21], and [24]). The helix formation is characterized by a steadily changing baseline over one orbit cycle. Fig. 1 shows the development of the vertical wavenumber  $\kappa_Z$  for one orbit cycle ( $360^\circ$ ) for the 12 full-performance TDX beams (each associated to a different look angle) in the first acquisition period (from September 8, 2011). The simulation of the orbit cycle starts from the equator ( $0^\circ$  latitude) in an ascending orbit pass, goes across the North Pole ( $90^\circ$  latitude), changes to a descending orbit pass, crosses the equator in a descending orbit pass ( $0^\circ$  latitude), passes the South pole ( $-90^\circ$  latitude), changes again to an ascending orbit pass, and crosses the equator again in an ascending orbit pass ( $0^\circ$  latitude). During one orbit cycle,  $\kappa_Z$  goes twice down to zero (no height sensitivity). This happens, depending on the used beam, in the northern hemisphere between  $35^\circ$  and  $75^\circ$  latitudes for the descending orbit pass and in the southern hemisphere between  $-40^\circ$  and  $-80^\circ$  latitudes for the ascending orbit pass. Meaningful (sensitive) acquisitions, as required for a successful height inversion, start from  $\kappa_Z > 0.05$  rad/m [10]. This means that, for the baseline configuration as displayed in Fig. 1, areas between  $35^\circ$  and  $75^\circ$  latitudes can

be only covered with a sensitive  $\kappa_Z$  in the ascending orbit pass, whereas the areas between  $-40^\circ$  and  $-80^\circ$  latitudes can be only covered with a sensitive  $\kappa_Z$  in the descending orbit pass. For all other areas, too, high or too low  $\kappa_Z$  values can be avoided by a proper selection of the beam (look angle). Decreasing the look angle increases  $\kappa_Z$  and vice versa.

Fig. 2 shows a plot of the development of  $\kappa_Z$  as a function of mission time for the years 2011 and 2012 (roughly covering the two acquisition periods) for the three test sites Krycklan, Traunstein, and Mawas (representing different arguments of latitude) in ascending and descending orbit pass. The plot was done for beam "strip\_008," which corresponds to a look angle of  $\sim 30.4^\circ$ .

The first acquisition period started in the beginning of February 2011. The abrupt increase in  $\kappa_Z$  at the beginning of April 2012 indicates the change between the first and second acquisition periods of the TDX mission. All other small peaks result from orbit adjustments due to acquisition needs.

For the Mawas site, which is located close to the equator, the difference in  $\kappa_Z$  between the ascending and descending orbit passes is small (red and orange lines in Fig. 2). However, for the Krycklan site (light blue and dark blue lines in Fig. 2) and the Traunstein site (light green and dark green lines in Fig. 2), the difference between the ascending and descending  $\kappa_Z$  is large. In the descending orbit pass,  $\kappa_Z$  was mostly lower than 0.05 rad/m for both sites. Only the Traunstein site could be covered with vertical wavenumbers larger than 0.05 rad/m from April 2012 until November 2012 in the descending orbit pass.

During the first acquisition period, almost all test sites could be acquired, in ascending mode, with baselines appropriate for forest structure investigation (i.e.,  $\text{HoA} > \text{maximum forest height}$ ). Only for the Traunstein site was  $\kappa_Z$  too large to cover the prevailing forest heights on the ground, but this problem could be overcome by choosing an acquisition at a larger incidence angle. In the second acquisition period, all test sites could be acquired, in ascending mode, with effective baselines that are in general too large ( $\kappa_Z > 0.2$  rad/m, corresponding to  $\text{HoAs} < 31$  m) to provide the sensitivity required for forest structure

estimation (coherence mostly insensitive). More appropriate baselines (with  $\kappa_Z$  values below 0.2 rad/m) appeared only after November 2012. In addition, here, acquisitions at larger incidence angles would decrease  $\kappa_Z$ .

The plot in Fig. 2 is limited to a single beam, and there was still potential to optimize  $\kappa_Z$  by a proper selection of the look angle. However, it shows also that a careful planning of an acquisition is necessary if a certain  $\kappa_Z$  is required.

### III. TEST SITES AND DATA SETS

In this paper, data from three forest sites representative of three key forest ecosystems (i.e., boreal, temperate, and tropical) characterized by very different forest and terrain conditions were used. All sites have been used in the past as test sites for airborne Pol-InSAR experiments. Actual airborne LIDAR measurements were available.

Cross validation was done on stand level homogeneous forest areas with a mean size of  $\sim 3$ – $5$  ha. Every stand is represented by its mean value. This is necessary to compensate for the residual spatial misregistration between SAR and LIDAR reference data, occurring when georeferencing both data sets. Of course, this averaging also reduces the variation of the obtained estimates.

From the LIDAR data, the forest canopy top height H100 was calculated and used as a reference. H100 is a standard parameter in forest mensuration and is defined as the mean height of the largest 100 trees per hectare [25]. H100 is considered to represent the upper height of the tree crowns in a forest.

Airborne LIDAR penetrates into the forest and therefore underestimates the top vegetation height [14], [15], [25]. An estimate of the forest top height H100 was obtained by taking the maximum LIDAR vegetation height within a  $10\text{ m} \times 10\text{ m}$  window. This allows compensating for the underestimation of the LIDAR forest height estimates [5], [27]. This method has been successfully used for small footprint ( $\sim 15$ -cm diameter) airborne LIDAR systems with  $\sim 1$  to  $\sim 4$  hits per square meter.

Even if the LIDAR and radar measurements were up to three years/growth periods apart, a proper cross validation was still possible as maximum possible forest height growth for this time period was, for most forest stands, on the order of  $\sim 1$  m or even below (see test site descriptions in Section III-A and B). Therefore, forest height changes due to growth were neglected in the cross validation. Large areas of wood harvest or naturally destroyed forest areas (caused by wind throw or forest fires) clearly appear as outliers in the validation plots.

The TDX data sets available and used for each site are summarized in Table I. The test sites are described in the following sections.

#### A. Krycklan Test Site

The Krycklan forest is located in central Sweden ( $64^\circ 10'$  north and  $20^\circ 01'$  east) and represents typical forest conditions for Scandinavian boreal forest systems. It is a managed forest with a mean forest height of 18 m and a mean biomass level of 90 t/ha. Maximum forest height measured is 30 m with a biomass of 220 t/ha. The forest is dominated by coniferous tree species (Norway spruce and Scots pine) with fractions of

TABLE I  
SUMMARY OF USED TDX AND E-SAR DATA

Test site	Date	Look angle [°]	$\kappa_Z$ [rad/m]	HoA [m]	Polarization	Mode
Krycklan	2010/07/28	32°	0.17	38	HH VV	ascending, Stripmap, pursuit monostatic
Krycklan	2010/12/17	19°	0.09	69	HH	descending, Stripmap, bistatic
Krycklan	2011/06/11	19°	0.05	125	HH	descending, Stripmap, bistatic
Traunstein	2012/01/09	43°	0.09	69	HH VV	ascending, Stripmap, bistatic
Traunstein	2009/06/09	25° -55°	0.14 -0.27	23 -46	VV	airborne (E-SAR), Stripmap, monostatic
Mawas	2011/08/25	31°	0.12	52	HH VV	descending, Stripmap, bistatic
Mawas	2011/12/13	31°	0.07	89	HH VV	descending, Stripmap, Bistatic
Mawas	2011/12/24	31°	0.07	89	HH VV	descending, Stripmap, bistatic
Mawas	2012/01/04	31°	0.08	79	HH VV	descending, Stripmap, bistatic

birch. The site has a hilly topography characterized by moderate slopes and a height variation between 20 and 400 m above mean sea level (AMSL).

Airborne LIDAR measurements were collected in late summer 2008. For cross validation, 252 homogeneous stands with a mean stand size of 3 ha were chosen. In terms of TDX data sets, three acquisitions were analyzed. One dual-pol (HH and VV) pursuit monostatic acquisition from July 2010 acquired with a 32° look angle from an ascending orbit (see Fig. 3), and two bistatic single-pol (HH) acquisitions acquired with a 19° look angle from a descending orbit in December 2010 and June 2011, respectively. All data were acquired in the stripmap mode.

The time between the LIDAR data acquisition and the last TDX data acquisition comprised three growth periods. The maximum height growth for this time period is  $\sim 1.2$  m (0.4 m per year), but only for trees with an age between 20 and 40 years ( $\sim 13$  m high) [28]. For all other trees (age classes), forest growth is below 1 m. Forest growth of approximately 1 m is below the sensitivity of the used methods and can therefore be neglected for cross validation at this site. For the cross validation of model-based forest height estimates (see Section V), only two growth periods need to be considered.

Fig. 3(a) shows the VV amplitude image of the July 2010 acquisition. The image dimension is approximately 18 km  $\times$  50 km. In Fig. 3(b), the interferometric coherence image is shown scaled from 0 (black) to 1 (white), and in Fig. 3(c) on the right, the associated TDX DEM is shown. The area covered by the LIDAR measurements is indicated by the black rectangle.

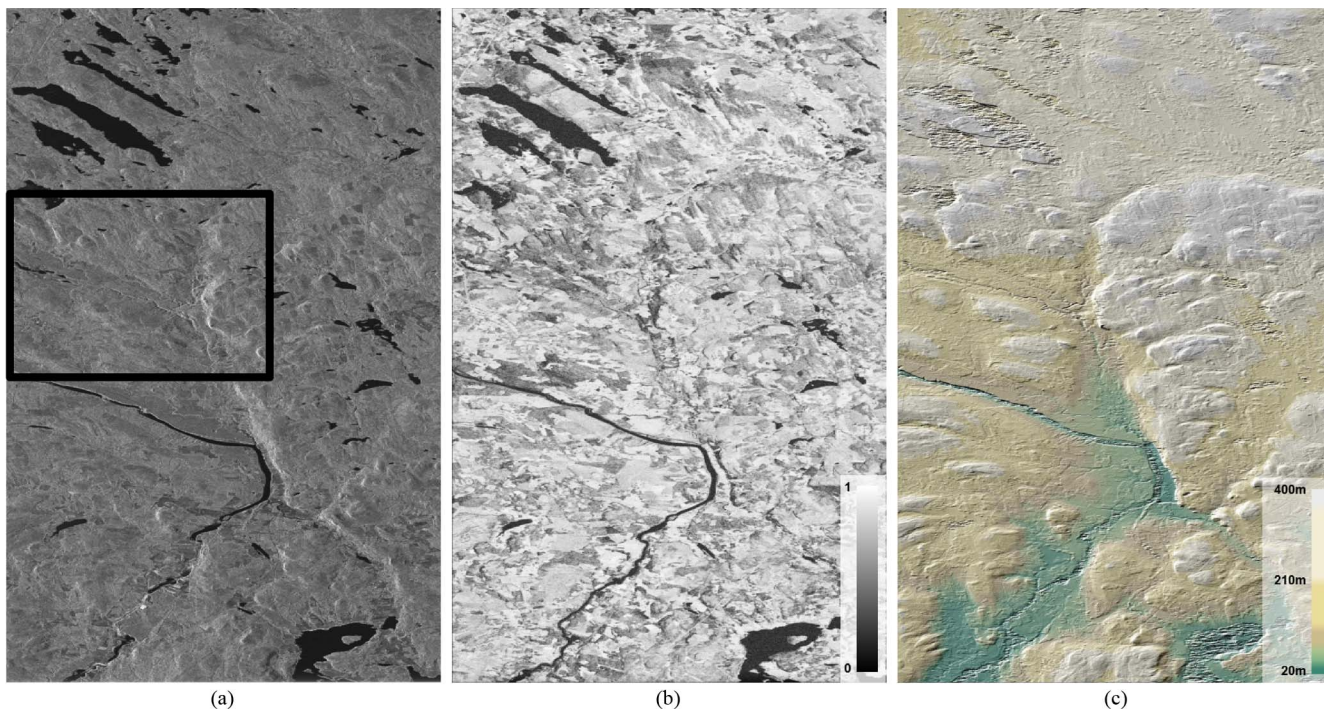


Fig. 3. Krycklan test site (July 28, 2010 acquisition). (a) VV amplitude image; the area covered by the LIDAR measurements is indicated by the black rectangle. (b) VV interferometric coherence scaled from 0 (black) to 1 (white). (c) TDX DEM scaled from 20 m (dark green) to 400 m (white). Image dimension:  $\sim 18$  km (range)  $\times$   $\sim 50$  km (azimuth).

### B. Traunstein Test Site

The Traunstein site is located in the southeast of Germany ( $47^{\circ}52'$  north,  $12^{\circ}39'$  east), east of the town Traunstein, in the prealpine moraine landscape of southern Germany.

The climatic conditions favor temperate mixed mountainous forest stands, dominated by Norway spruce, beech, and fir. It is a managed forest composed of even-aged stands (mainly older forest parts) and mixed uneven-aged stands (mainly younger forest parts) with forest heights from 10 up to 40 m and higher. Mean biomass level is on the order of 210 t/ha; individual old forest stands can reach biomass levels up to 600 t/ha (above average compared with other temperate forests). The topography of the site varies from 530 to 650 m AMSL, with only a few steep slopes.

Airborne LIDAR height measurements were performed in the summer of 2008. For cross validation, 22 homogeneous stands with a mean stand size of  $\sim 3$  ha were chosen. In terms of TDX, only one stripmap bistatic dual-pol (HH and VV) acquisition acquired with a  $42^{\circ}$  look angle from an ascending orbit in January 2012 was investigated. During the acquisition, the scene was covered with an  $\sim 0.3$ -m-thick snow layer. Additionally, an airborne summer acquisition from June 2009 acquired at X-band in a single-pass interferometric mode in VV polarization by the E-SAR system of DLR [29], [30] was analyzed to evaluate differences in backscattering between summer and winter conditions. Here, as in the Krycklan test site, the time difference between the LIDAR data acquisition and the TDX data acquisition comprised three growth periods.

Under the growth conditions in Traunstein, the maximum height growth within three years is  $\sim 1.9$  m (0.63 m per year) for trees in the age between 20 and 40 years ( $\sim 17$  m high), reduces

to  $\sim 0.9$  m for trees in the age of 60 years ( $\sim 30$  m high), and reduces even more for trees older than 80 years [28]. As most of the validation stands were larger than 20 m and forest growth of  $\sim 1$  m is below the sensitivity of the used methods, forest growth was neglected for cross validation at this site.

Fig. 4(a) shows the VV amplitude image of the TDX data. The image dimension is approximately  $18$  km  $\times$   $15$  km. In Fig. 4(b), the interferometric coherence image is shown scaled from 0 (black) to 1 (white), and in Fig. 4(c) the associated TDX DEM is shown. The area covered by the LIDAR measurements is indicated by a black rectangle.

### C. Mawas Test Site

The Mawas site is an Indonesian forest conservation area located in Central Kalimantan ( $-2^{\circ}09'$  south and  $114^{\circ}27'$  east). It is covered with a tropical peat swamp forest that is still marked by strong logging activities carried out in the early 90s of the last century. Logging tracks are still visible today—on the ground and on the LIDAR and SAR data. Two forest types can be distinguished in the test site, namely, riverine forest in the proximity of the river and peat swamp forest covering the rest of the scene (see Fig. 5).

Typical for the Mawas site is the distinct change between dry and wet seasons: At the end of the wet season, the forest is widely flooded, whereas at the peak of the dry season, the trees partly drop off their leaves to endure the lack of water [5]. Forest height reaches up to 30 m; the mean biomass is around 200 t/ha with maximum values up to 300 t/ha. The terrain topography is rather flat and slowly varies from 5 to 50 m AMSL across the whole scene. A detailed description of the Mawas test site is given in [5] and [31].

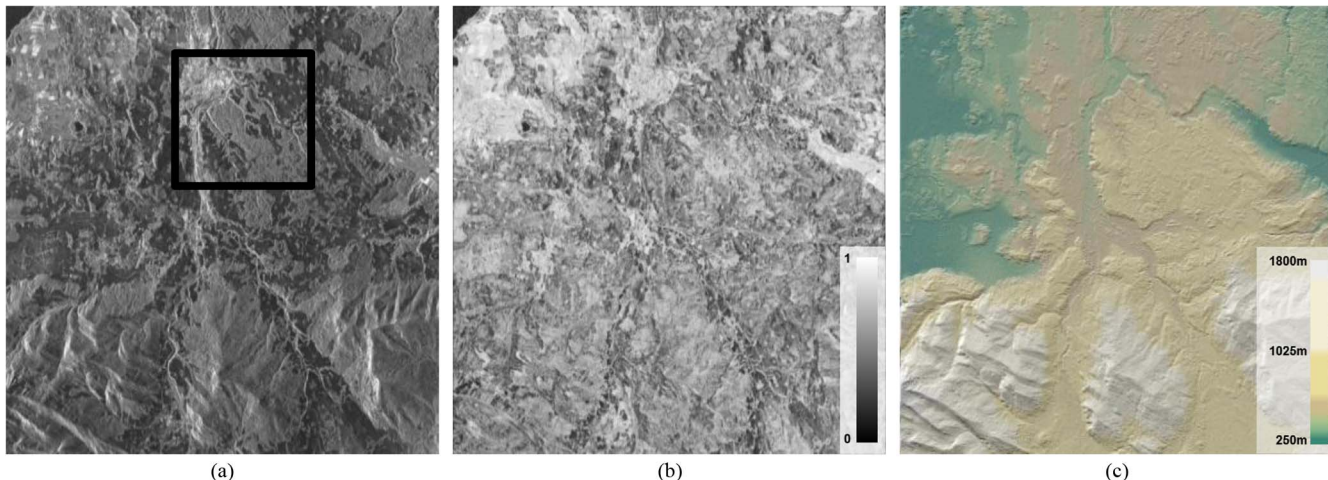


Fig. 4. Traunstein test site (August 25, 2011 acquisition). (a) VV amplitude image; the area covered by the LIDAR measurements is indicated by the black rectangle. (b) VV interferometric coherence scaled from 0 (black) to 1 (white). (c) TDX DEM scaled from 250 m (dark green) to 1800 m (white). Image dimension:  $\sim 18$  km (range)  $\times$   $\sim 15$  km (azimuth).

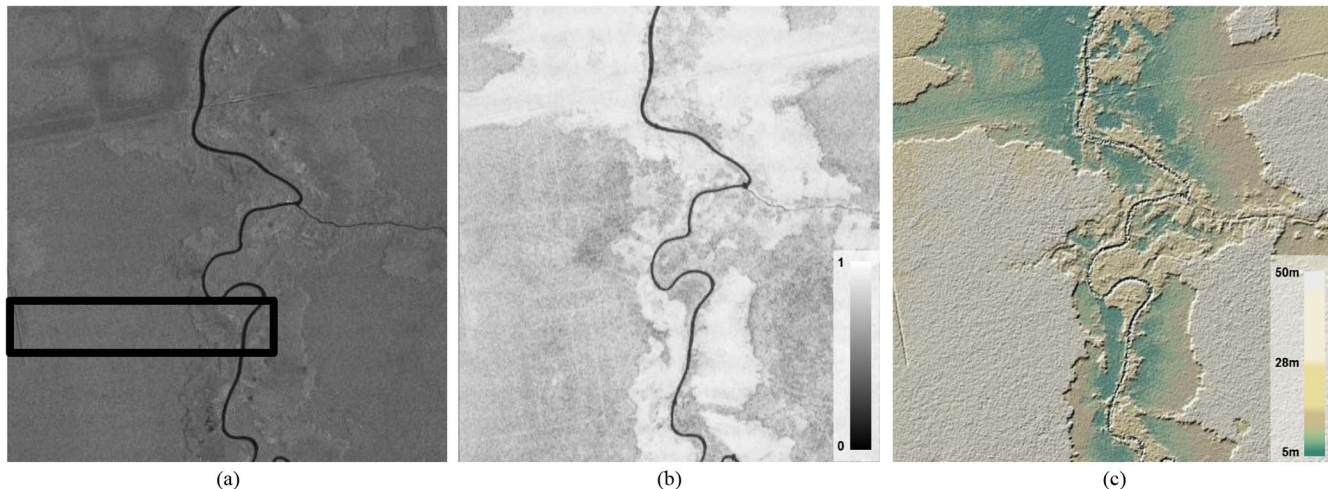


Fig. 5. Mawas test site (August 25, 2011 acquisition). (a) VV amplitude image; the area covered by the LIDAR measurements is indicated by the black rectangle. (b) VV interferometric coherence scaled from 0 (black) to 1 (white). (c) TDX DEM scaled from 5 m (dark green) to 50 m (white). Image dimension:  $\sim 20$  km (range)  $\times$   $\sim 20$  km (azimuth).

In August 2011, airborne LIDAR measurements were performed with a swath width of about 500 m crossing the TDX images. The LIDAR strip was divided for cross validation into 100 parts of equal size with an area of  $\sim 4.5$  ha, and each part is assigned one H100 value. For this site, a time series of four stripmap bistatic dual-pol (HH and VV) acquisitions acquired with a  $31^\circ$  look angle from a descending orbit in summer and late autumn/winter 2012 has been investigated.

The first acquisition is from August 25, 2011 (peak of dry season), followed by three acquisitions separated by 11 days on December 13 (start of the rainy season), December 24, and January 4, 2012. LIDAR measurements and TDX acquisitions took place in the same year so that no significant forest changes between the LIDAR and TDX acquisitions are expected.

Fig. 5(a) shows the VV amplitude image from the August 2011 acquisition. The image dimension is approximately  $20$  km  $\times$   $20$  km. In Fig. 5(b), the interferometric coherence image is shown scaled from 0 (black) to 1 (white), and Fig. 5(c) shows the associated TDX DEM. In the DEM, the flatness

of the area becomes obvious; the largest height changes are induced by changes in vegetation height. The area covered by the LIDAR measurements is indicated by the black rectangle.

#### IV. X-BAND FOREST HEIGHT ESTIMATION PERFORMANCE

Feasibility and performance of forest Pol-InSAR applications at X-band critically depend on two effects.

- 1) The capability of X-band to penetrate into and through the forest: The penetration is required in order to “see” enough from the forest volume: The maximum vegetation height that can be resolved is given by the penetration depth. With further increasing height, the interferometer does not see anymore the whole volume, and the height estimation “saturates.” The penetration capability depends in general on the density and dielectric properties of the forest/canopy layer. Both parameters vary spatially and in time for many forest types in a seasonal cycle.

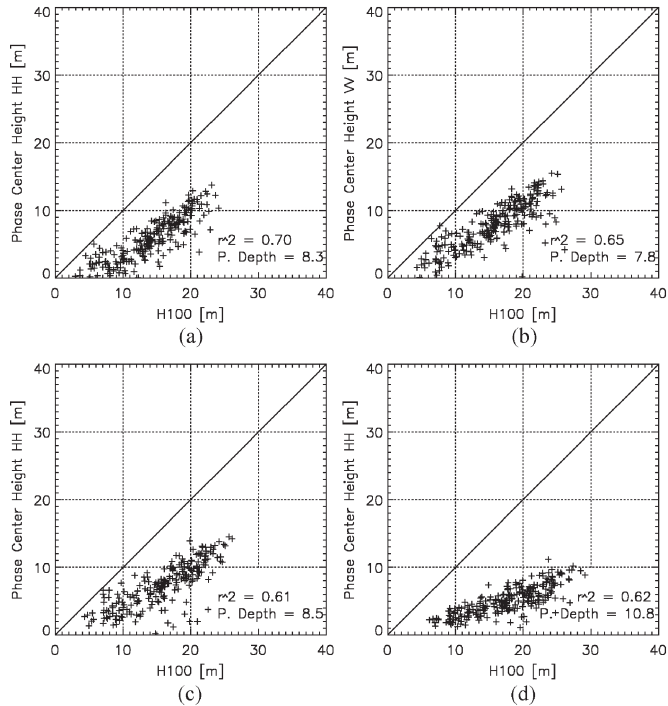


Fig. 6. Krycklan test site validation plots: phase center height versus LIDAR forest height for different polarizations, look angles, and seasons. (a) HH polarization acquired in July 2010 with look angle =  $32^\circ$ . (b) VV polarization acquired in July 2010 with look angle =  $32^\circ$ . (c) HH polarization acquired in June 2011 with look angle =  $19^\circ$ . (d) HH polarization acquired in December 2010 with look angle =  $19^\circ$ .

- 2) The dependence of the interferometric coherence (in amplitude and phase) on the polarization(s) of the images is used to form the interferogram. This again depends on the polarimetric properties of the individual scatterers and their distribution in height. Reduced polarization dependence indicates a limit in the information content of the Pol-InSAR observation space, reducing the value of the polarimetric diversity in interferometric measurements.

Both effects are investigated in the following sections.

#### A. Penetration Depth

In order to establish the penetration depth in the forest volume, the height difference between the available LIDAR DTM and the X-band DEM (corresponding to the interferometric phase center height) was estimated for each TDX data set for all stands available in the three test sites and plotted against the individual LIDAR H100 forest height. For each plot, the correlation coefficient, i.e.,  $r^2$ , and the mean penetration depth were calculated.

1) *Krycklan Test Site*: The plots for the Krycklan site are shown in Fig. 6. Fig. 6(a) corresponds to the HH polarization of the (monostatic) summer (July 2011) acquisition with a  $32^\circ$  look angle, and Fig. 6(b) corresponds to the VV polarization of the same acquisition. For both polarizations, the phase center height is close to half the forest height, indicating a low extinction level for this test site. The comparison of the plots makes it clear that the HH phase centers, characterized by a penetration

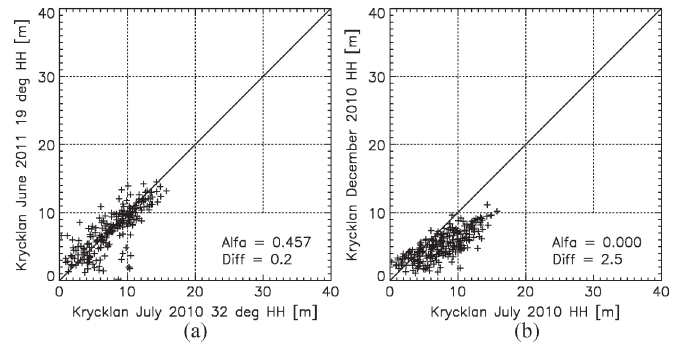


Fig. 7. Krycklan test site phase center heights comparison. (a) HH polarization acquired in July 2010 with look angle =  $32^\circ$  versus HH polarization acquired in June 2011 with look angle =  $19^\circ$ . (b) HH polarization acquired in July 2010 with look angle =  $32^\circ$  versus HH polarization acquired in December 2010 with look angle =  $32^\circ$ ; Alfa is the significance, a value between 0 and 1. A small value (up to 0.01) indicates significantly different means. Diff is the mean difference in meters between the two phase center heights.

depth of 8.3 m, are, on average, located 0.5 m “deeper” than the corresponding VV phase centers, characterized by a penetration depth of 7.8 m.

This difference can be interpreted by a (slightly) higher ground contribution in the HH polarization than in the VV polarization.

Fig. 6(c) corresponds to the HH polarization of the second (bistatic) summer (June 2011) acquisition acquired at a steeper look angle of  $19^\circ$ . The phase centers are located at comparable heights as in the July acquisition [see Fig. 6(a)] acquired with a shallower  $32^\circ$  look angle at comparable penetration depth levels (8.5 m at  $19^\circ$  look angle in June versus 8.3 m at  $32^\circ$  look angle in July). The small difference in penetration between the two look angles implies that this look angle difference of  $13^\circ$  has a rather minor effect on the location of the scattering centers.

Fig. 6(d) corresponds to the HH polarization of the December 2010 acquisition acquired with the same mode and geometry (i.e.,  $19^\circ$  look angle) as the June 2011 acquisition [see Fig. 6(c)]. The comparison of the winter and summer plots [see Fig. 6(c) and (d)] shows a significant lower phase center location, indicating a larger penetration in the winter (10.8 m) than in the summer (8.3 m). A possible interpretation is an increased ground scattering contribution as a consequence of the frozen vegetation conditions (decreased vegetation dielectric constant) combined with the loss of leaves. Both effects decrease volume attenuation.

Fig. 7(a) shows a plot of phase center heights in HH polarization acquired in July 2010 with a  $32^\circ$  look angle versus the phase center heights in HH polarization acquired in June 2011 with a  $19^\circ$  look angle, and Fig. 7(b) shows a plot of phase center heights in HH polarization acquired in July 2010 with a  $32^\circ$  look angle versus the phase center heights in HH polarization acquired in December 2010 with a  $32^\circ$  look angle. The significance of the difference in phase center height was tested with the  $t$ -test (Student’s  $t$  distribution). The difference of the phase center heights between  $19^\circ$  and  $32^\circ$  look angles appears not to be significant, but the difference of the phase center heights between the July and December acquisitions is highly significant.

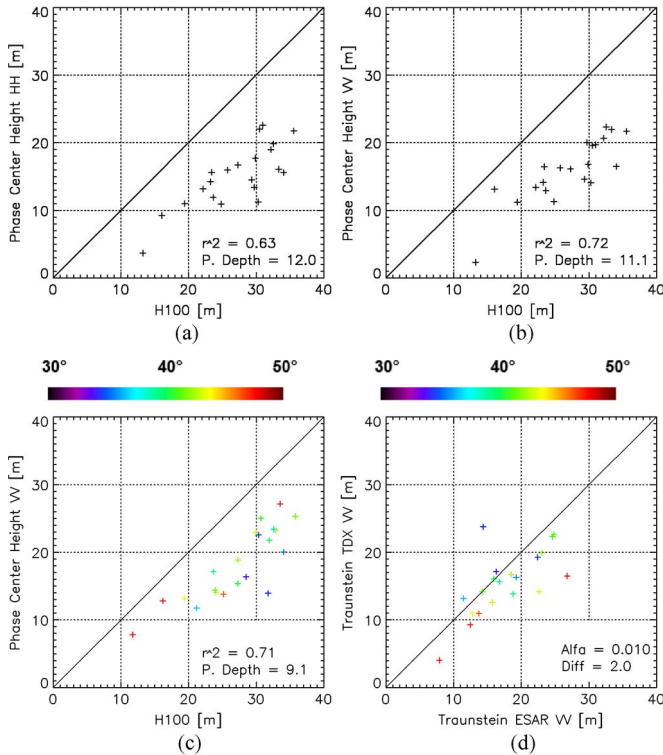


Fig. 8. Traunstein test site validation plot: phase center height versus LIDAR forest height. (a) TDX data in HH polarization acquired in January 2012 with a  $45^\circ$  incidence angle. (b) TDX data in VV polarization acquired in January 2012 with a  $45^\circ$  incidence angle. (c) E-SAR airborne data in VV polarization acquired in June 2009 (plot is color-coded according to the mean incidence angle of the stands). (d) Phase center heights comparison: E-SAR VV polarization acquired in June 2009 versus TDX VV polarization acquired in January 2012 with a  $45^\circ$  incidence angle (plot was color-coded according to the mean incidence angle of the stands in the E-SAR acquisition). Alfa is the significance, a value between 0 and 1. A small value (up to 0.01) indicates significantly different means. Diff is the mean difference in meters between the two phase center heights.

2) *Traunstein Test Site*: The phase center height plots for the single acquisition over the Traunstein site acquired in January 2012 are shown in Fig. 8. Fig. 8(a) shows the HH and Fig. 8(b) the VV phase center heights plotted against the forest height for each available validation stand. Similar to the observations in Krycklan, in Traunstein, the HH polarization phase centers characterized by a 12-m mean penetration depth are located, on average, 0.9 m closer to the ground than the VV phase centers (characterized by an 11.1-m penetration depth). In the absence of a suitable TanDEM-X summer acquisition, a data set acquired by the airborne E-SAR system of DLR in June 2009 was used to evaluate the seasonal behavior of the site. The corresponding phase center height plot is shown in Fig. 8(c) (the plot is color-coded according to the mean incidence angle of the stands) and indicates about 2 m higher located phase centers (characterized by a 9.1-m penetration depth). This underlines again the different penetration depths in summer and winter. However, compared with the Krycklan site, the phase center height is located in Traunstein—even in winter—clearly above the half forest height reflecting the denser forest conditions of this test site.

A direct comparison between the phase center heights of the TDX acquisition from January 2012 and the phase center

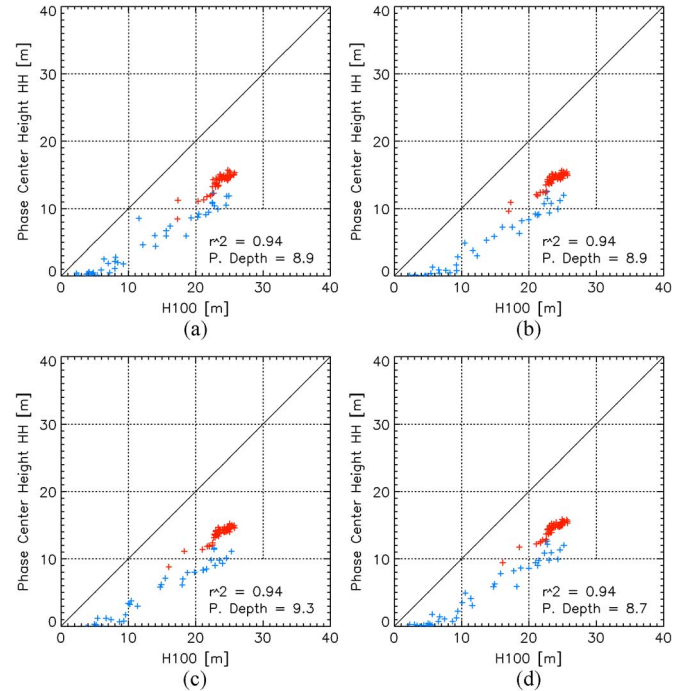


Fig. 9. Mawas test site validation plot: phase center height versus LIDAR forest height in HH polarization. (a) August 25, 2011. (b) December 13, 2011. (c) December 24, 2012. (d) January 4, 2012. (Blue dots) Riverine forest. (Red dots) Peat swamp forest.

heights of the E-SAR acquisition from June 2009 is shown in Fig. 8(d) (the plot is color-coded according to the mean incidence angle of the stands in the E-SAR acquisition; incidence angle in the TDX acquisition was considered constant). The  $t$ -test indicates that the difference in phase center height is highly significant. Only stands with a steeper incidence angle in the E-SAR acquisition than in the TDX acquisition have a higher phase center height in the winter than in the summer ( $35^\circ$  in case of E-SAR versus  $45^\circ$  in case of TDX). In this constellation, the incidence angle seems to affect the position of the phase center height. A steeper incidence angle seems to lower the phase center height, i.e., allowing a deeper penetration. However, here, the results need to be carefully interpreted as incidence angle effects and seasonal effects mix up.

3) *Mawas Test Site*: The phase center height plots for the four available bistatic acquisitions (see Table I), i.e., one acquired in summer 2011 (dry season) and three in winter 2011–2012 (at the beginning of the wet season), are shown in Fig. 9 for the HH polarization and in Fig. 10 for the VV polarization.

The penetration depth changed only marginally from acquisition to acquisition and between polarizations. However, there seems to be a decrease in penetration depth between wet and dry seasons. In addition, for the Mawas site, the height of the phase center was with penetration depths ranging from 8.5 m (VV polarization from January 4, 2012) to 9.4 m (VV polarization from August 25, 2011) clearly below the forest canopy.

In the phase center height plots (see Figs. 9 and 10), the two forest types (riverine forest and peat swamp forest) of the scene can be clearly identified.

The riverine forest is displayed with blue dots in Figs. 9 and 10, and the peat swamp forest is displayed with red dots.

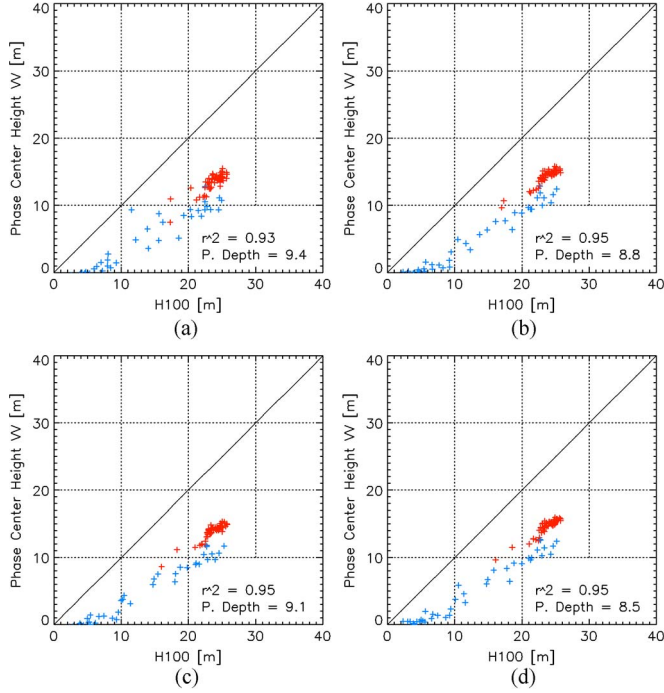


Fig. 10. Mawas test site validation plot: phase center height versus LIDAR forest height in VV polarization. (a) August 25, 2011. (b) December 13, 2011. (c) December 24, 2012. (d) January 4, 2012. (Blue dots) Riverine forest. (Red dots) Peat swamp forest.

### B. Polarimetric Diversity

The polarimetric diversity of the interferometric coherence is established by the coherence region concept [1]. In the case of a dual-pol InSAR configuration operating in HH and VV, a 2-D scattering vector  $\vec{k}_1 = [S_{HH}^1 \ S_{VV}^1]^T$  and  $\vec{k}_2 = [S_{HH}^2 \ S_{VV}^2]^T$  is acquired at each end of the (spatial) baseline, where  $S_{JJ}^i$  are the copolarized (complex) scattering amplitudes of the corresponding scattering matrix. The scattering amplitude  $S(\vec{w})$  of any polarization state  $\vec{w}$  in the 2-D subspace defined by  $S_{HH}$  and  $S_{VV}$  can be defined by the projection of the scattering vector  $\vec{k}$  on the unitary complex vector  $\vec{w}$  as [1]

$$S_1(\vec{w}) := \vec{w}^+ \cdot \vec{k}_1 \quad S_2(\vec{w}) := \vec{w}^+ \cdot \vec{k}_2. \quad (2)$$

The interferometric coherence is then given by

$$\tilde{\gamma}(\kappa_z, \vec{w}) = \frac{\vec{w}^+ [\Omega_{12}(\kappa_z)] \vec{w}}{\sqrt{(\vec{w}^+ [T_{11}] \vec{w}) (\vec{w}^+ [T_{22}] \vec{w})}} \quad (3)$$

where

$$\begin{aligned} [\Omega_{12}(\kappa_z)] &:= \langle \vec{k}_1 \cdot \vec{k}_2^T \rangle & [T_{11}] &:= \langle \vec{k}_1 \cdot \vec{k}_1^T \rangle \\ [T_{22}] &:= \langle \vec{k}_2 \cdot \vec{k}_2^T \rangle. \end{aligned}$$

Using its polar form, the interferometric coherence  $\tilde{\gamma}(\kappa_z, \vec{w})$  can be represented on the unit circle (see Fig. 11) by a point with radius  $0 \leq |\tilde{\gamma}(\kappa_z, \vec{w})| \leq 1$  and phase  $\varphi = \arg\{\tilde{\gamma}(\kappa_z, \vec{w})\}$  [4].

The region on the unit circle defined by the loci of the interferometric coherences  $\tilde{\gamma}(\kappa_z, \vec{w}_i)$  for all possible  $\vec{w}_i$  is called the coherence region (red ellipse in Fig. 11) and is used to interpret the polarimetric interferometric signature of the

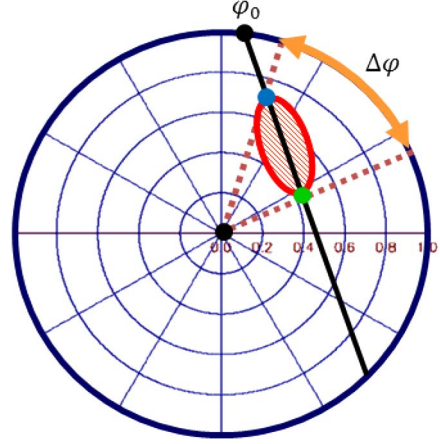


Fig. 11. (Red ellipse) Unit circle with coherence region. (Blue dot)  $\tilde{\gamma}_{\text{Vol}}(\vec{w}_{\text{max}})$ . (Green dot)  $\tilde{\gamma}_{\text{Vol}}(\vec{w}_{\text{min}})$ . (Black dot) ground phase  $\varphi_0$ . (Double-headed arrow) Maximum phase difference  $\Delta\varphi$ .

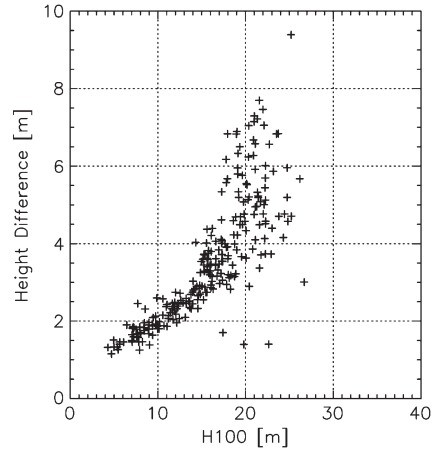


Fig. 12. Krycklan test site validation plot: polarimetric phase height  $\Delta h$  difference versus LIDAR forest height for the TDX dual-pol acquisition from July 2010.

underlying scatterer. The radial extent of the coherence region indicates the variation of the absolute value of the interferometric coherence as a function of polarization. The angular extent of the coherence region indicates the variance of the interferometric phase (center) as a function of polarization. The maximum phase difference  $\Delta\varphi$  established by the coherence region indicates the maximum variation of the interferometric phase (center) obtained by changing the polarization of the images used to form the interferogram, and it can be converted to a (baseline independent) height difference  $\Delta h$  by scaling with the vertical wavenumber, i.e.,  $\Delta h = \Delta\varphi/\kappa_z$ . Large  $\Delta\varphi$  values indicate the presence of (polarized) scattering contributions at different heights within the scattering volume. However, a note of caution is required when interpreting the interferometric coherence on the unit circle: the estimation of both the absolute value and the argument of the interferometric coherence is affected by an inherent variance defined by the (absolute) coherence value and the number of looks used for its estimation [33].

1) *Krycklan Test Site*: In Fig. 12, the maximum phase difference  $\Delta\varphi$  (scaled to a maximum height difference  $\Delta h$ ) estimated from the dual-pol July 2010 acquisition (see Table I)

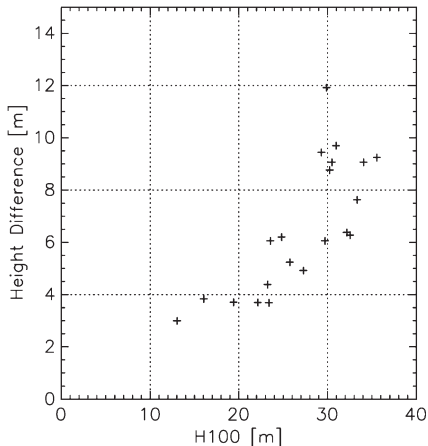


Fig. 13. Traunstein test site validation plot: polarimetric phase height difference  $\Delta h$  versus LIDAR forest height for the dual-pol acquisition from January 2012.

is plotted against the LIDAR-derived H100 (i.e., top forest height) for each of the validation stands in Krycklan. The height difference  $\Delta h$  increases with increasing forest height (2–3 m in 10-m-tall stands to 6–8 m in 25-m-tall stands), which points, as expected, to a larger height difference between the interferometric phase centers in higher stands than in lower. At the same time, with increasing forest height, the variance of the polarimetric distance increases due to the variation in density.

2) *Traunstein Test Site*: The corresponding plot for the Traunstein site, i.e., the maximum height difference  $\Delta h$  estimated from the dual-pol acquisition of January 2012 (see Table I), for each validation stand plotted against the corresponding LIDAR derived H100, is shown in Fig. 13. Also in this case  $\Delta h$  (and its variance) increases with increasing forest height: 2 m to 4 m for forest stands with heights between 10 m to 20 m up to 8 m to 10 m for stands of about 35 m.

3) *Mawas Test Site*: Finally, the maximum height difference  $\Delta h$  estimated for each validation stand plotted against the corresponding LIDAR-derived H100 for the Mawas site for all four available dual-pol acquisitions (see Table I) is shown in Fig. 14. Fig. 14(a) corresponds to the August acquisition in the dry season, Fig. 14(b) and (c) corresponds to the acquisition from December 13 and 24, 2011, and Fig. 14(d) corresponds to the acquisition from January 4, 2012, of the wet season.

Compared with the European test sites, the dependence of  $\Delta h$  on forest height was less pronounced in the Mawas case. The two forest classes (riverine forest = blue dots in Fig. 14 and peat swamp forest = red dots in Fig. 14) separated in the phase center height plots can be also separated in the  $\Delta h$  plots.

In the dry period (August acquisition),  $\Delta h$  is about 2 m for the lower forest parts (< 10 m) and 3–4 m for the higher forest parts (> 20 m). In the rainy season (December and January acquisitions),  $\Delta h$  increases for all forest heights by approximately 1 m:  $\Delta h$  is now about 3 m for the lower forest parts and 4–5 m for the higher forest parts.  $\Delta h$  is stable for all three acquisitions in the rainy season (i.e., the two in December and the one in January). Compared with the European test sites (Krycklan and Traunstein), Mawas is characterized by smaller  $\Delta h$  levels, particularly for the taller forest fractions.

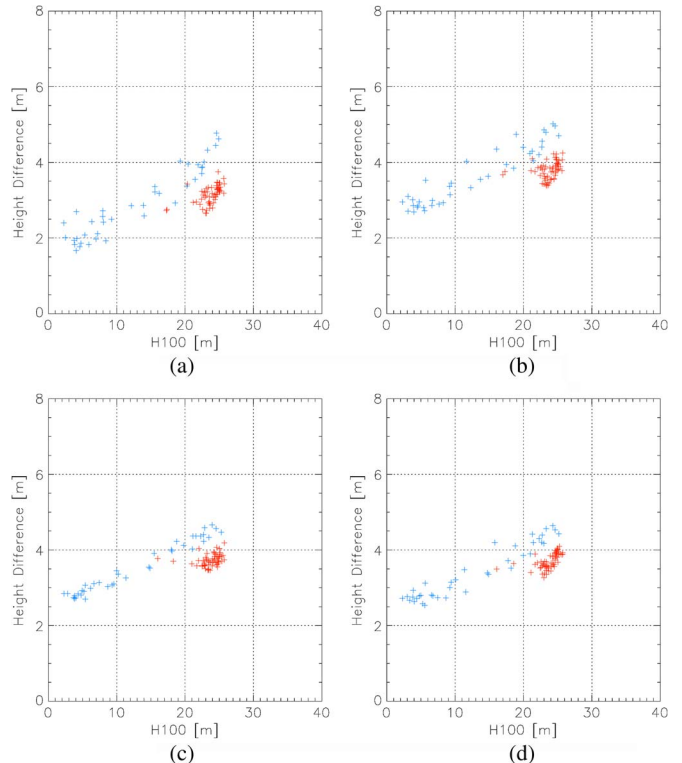


Fig. 14. Mawas test site validation plots: polarimetric phase height difference  $\Delta h$  versus LIDAR forest height. (a) August 25, 2011. (b) December 13, 2011. (c) December 24, 2012. (d) January 4, 2012. (Blue dots) Riverine forest (Red dots) Peat swamp forest.

## V. DATA INVERSION

Having established the two main preconditions, i.e., sufficient penetration into the forest volume and the polarimetric diversity of the interferometric coherence measurements over all test sites, the inversion of Pol-InSAR TDX data is discussed here. In forest Pol-InSAR applications, the volume decorrelation contribution of the interferometric coherence  $\tilde{\gamma}_{\text{Vol}}(\kappa_Z \vec{w})$  measured at a given spatial baseline  $\kappa_Z$  and at a given polarization  $\vec{w}$  can be modeled in terms of a two-layer model, the so-called random volume over ground (RVoG) model. Accordingly, the RVoG model consists of a polarization-independent vertical distribution of scatterers  $f_V(z)$  that accounts for the forest canopy (scattering and propagation) contribution and a Dirac-like component  $m_G(\vec{w})\delta(z - z_0)$  that accounts for the direct and dihedral (scattering) contribution(s) of the underlying ground [1]–[3], [34]. For monostatic configurations

$$\tilde{\gamma}_{\text{Vol}}(\kappa_Z, \vec{w}) = \exp(i\varphi_0) \frac{\tilde{\gamma}_V(\kappa_Z) + m(\vec{w})}{1 + m(\vec{w})} \quad (4)$$

with

$$\tilde{\gamma}_V(\kappa_Z) = \frac{\int_0^{h_V} f_V(z) \exp(i\kappa_Z z') dz'}{\int_0^{h_V} f_V(z) dz'}$$

where  $h_V$  is the top height of the forest volume corresponding to the forest top height H100,  $\varphi_0 = \kappa_Z z_0$  is the phase related to the ground topography  $z_0$ , and  $m(\vec{w}) = m_G(\vec{w}) / \int_0^{h_V} f_V(z) dz'$  is the effective ground-to-volume amplitude ratio. In the case of bistatic configurations, the direct and dihedral

contributions of the underlying ground are no longer equivalent [1], [35]: While the direct ground contribution remains deterministic (i.e., associated to a coherence that, after range spectral filtering, is equal to 1), the dihedral contribution becomes distributed in height and thus affected by volume decorrelation

$$\tilde{\gamma}_{\text{Vol}}(\kappa_Z, \vec{w}) = \exp(i\varphi_0) \frac{\tilde{\gamma}_V(\kappa_Z) + m_S(\vec{w}) + m_D(\vec{w}) \frac{\sin(\kappa_Z h_v)}{(\kappa_Z h_v)}}{1 + m_S(\vec{w}) + m_D(\vec{w})} \quad (5)$$

where  $m_S$  is the direct ground (surface) contribution, and  $m_D$  is the dihedral scattering contribution. However, the small bistatic angle of TanDEM-X combined with the rather low dihedral scattering contributions at X-band (when compared with lower frequencies) legitimizes the use of (4) instead of (5).

Different parameterizations of the vertical distribution of scatterers in the vegetation layer  $f_V(z)$  have been proposed and used in literature. A widely and very successfully used approach—particularly at higher frequencies—is to assume an exponential distribution of scatterers [4], [6], [7], [12], i.e.,

$$f_V(z) = \exp(2\sigma z / \cos(\theta_0)) \quad (6)$$

where  $\sigma$  describes the shape of the vertical distribution of scatterers, but it can be also interpreted as a mean extinction value that defines the attenuation rate of the vegetation layer. The high attenuation regime at X-band allows both interpretations, making the validation of  $\sigma$  ambiguous, particularly at the rather high spatial resolution scale of the TanDEM-X data.

The challenge now is the estimation of forest height  $h_V$  or other associated structure parameters used to parameterize  $f_V(z)$  from  $\tilde{\gamma}_{\text{Vol}}(\kappa_Z, \vec{w})$  measurements at different polarizations and (spatial) baselines by means of (4). The achieved performance critically depends on two steps. The first step is the estimation of the volume decorrelation contribution  $\tilde{\gamma}_{\text{Vol}}(\kappa_Z, \vec{w})$  from the overall measured interferometric coherence by compensating for all other (nonvolumetric) decorrelation contributions. The second step is to establish a balanced and well-conditioned inversion problem based on the available observation space, introducing—if required—additional assumptions and/or external information. Both steps for the TDX case will be discussed in the next sections.

### A. Coherence Calibration

A detailed overview of the relevant decorrelation contributions occurring in the case of TDX is provided in [20]. In the bistatic TDX mode, after range spectral filtering [36], the main nonvolumetric decorrelation contribution that has to be compensated is the additive noise decorrelation  $\gamma_{\text{SNR}}$ . The standard TDX data products [22] contain the noise equivalent sigma zero (NESZ) patterns for each channel in the form of a set of polynomial coefficients for one range line. Every  $\sim 1.5$ - to  $\sim 2$ -s azimuth time (acquisition dependent), a new set of polynomial coefficients is provided. They depend on the beam used for the acquisitions, the polarization, and the satellite. Fig. 15 shows an example of the NESZ pattern for the beam strip\_008 at HH and VV polarizations for TDX and TSX (from the Krycklan monostatic acquisition on July 28, 2010). TDX has, in near and far ranges [ $\sim -22$  dB; see Fig. 15(a) and (b)], about 1 dB lower

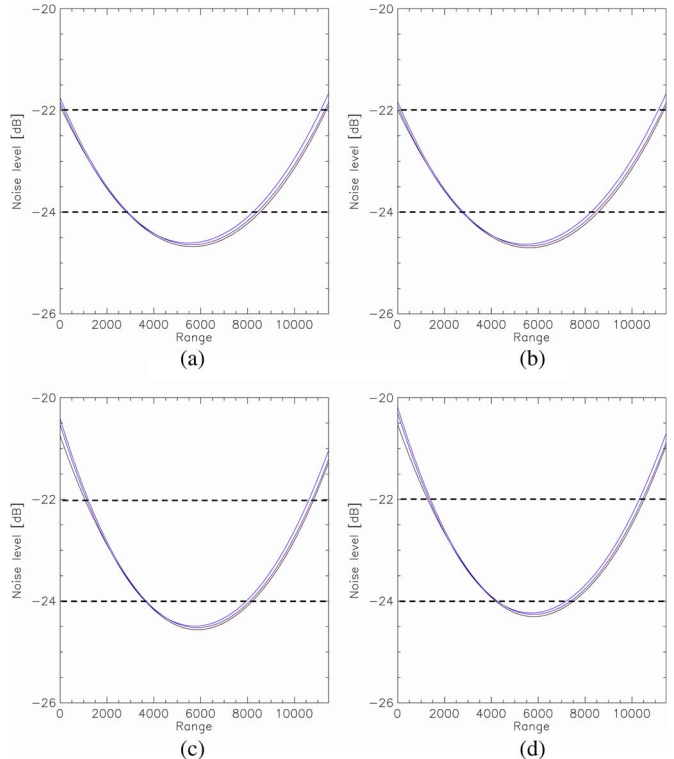


Fig. 15. Noise pattern for both polarizations of both satellites: five measurements along azimuth per channel (example monostatic acquisition over Krycklan on July 28, 2010, beam strip\_008). (a) TDX HH polarization. (b) TDX VV polarization. (c) TSX HH polarization. (d) TSX VV polarization.

noise level than TSX [ $\sim -21$  dB; see Fig. 15(c) and (d)]. The difference in midrange is below  $\sim 0.5$  dB. The noise level of TDX in HH polarization is nearly identical with the noise level in VV polarization [see Fig. 15(a) and (b)]. In case of TSX, the noise level in midrange is about 0.3 dB lower in the HH channel [ $\sim -24.5$  dB; see Fig. 15(c)] than in the VV channel [ $-24.2$  dB; see Fig. 15(d)].

For each channel, the signal-to-noise ratio (SNR) can be calculated by using the corresponding NESZ pattern and estimating the backscattering coefficient sigma nought  $\sigma_0$ , i.e.,

$$\text{SNR}^{\text{Pol Sat}} = \frac{\sigma_0^{\text{Pol Sat}} - \text{NESZ}^{\text{Pol Sat}}}{\text{NESZ}^{\text{Pol Sat}}} \quad (7)$$

where Pol indicates the polarization channel, and Sat is TDX or TSX. The SNR-induced decorrelation in the corresponding TDX interferogram is then obtained as [33]

$$\gamma_{\text{SNR}}^{\text{Pol}} = \frac{1}{\sqrt{\left(1 + \frac{1}{\text{SNR}^{\text{Pol TSX}}}\right) \left(1 + \frac{1}{\text{SNR}^{\text{Pol TDX}}}\right)}} \quad (8)$$

and is used to calibrate the interferometric coherence:  $\tilde{\gamma}_{\text{Vol}}(\kappa_Z, \text{Pol}) = \tilde{\gamma}(\kappa_Z, \text{Pol}) / \gamma_{\text{SNR}}^{\text{Pol}}$ . Fig. 16(a) and (c) shows the histograms of the obtained  $\gamma_{\text{SNR}}^{\text{Pol}}$  for the HH and VV polarizations, and Fig. 16(b) and (d) shows the histograms of the interferometric coherence before (red) and after (blue) correcting for  $\gamma_{\text{SNR}}^{\text{Pol}}$  for the Krycklan monostatic acquisition (July 28, 2010).

The mean noise decorrelation is about 0.95 for the HH channel and 0.93 for the VV channel and needs to be corrected

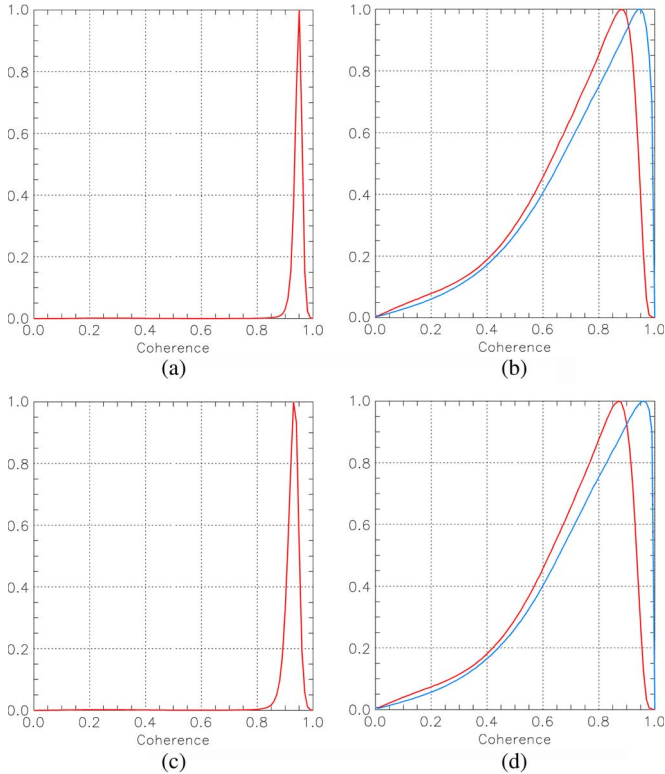


Fig. 16. Noise decorrelation (example monostatic acquisition over Krycklan on July 28, 2010). (a) Histograms of noise decorrelation  $\gamma_{SNR}^{HH}$ . (b) Histograms of the interferometric coherence before (red) and after (blue)  $\gamma_{SNR}^{HH}$  correction in HH polarization. (c) Histograms of noise decorrelation  $\gamma_{SNR}^{VV}$ . (d) Histograms of the interferometric coherence before (red) and after (blue)  $\gamma_{SNR}^{VV}$  correction in VV polarization.

for a successful Pol-InSAR height inversion [10]. After  $\gamma_{SNR}^{Pol}$  compensation, the interferometric coherences are ready to be used for inversion.

### B. Dual-Pol Inversion

In the case of a dual-polarimetric TDX acquisition, the parameterization of the two interferometric coherences in terms of (4) requires five parameters: the forest height  $h_V$ , the extinction  $\sigma$ , the ground topography phase  $\varphi_0$ , and the two ground-to-volume amplitude ratios  $m(\vec{w})$ , one for each polarization. A balanced inversion problem can be achieved by assuming a zero ground-to-volume amplitude ratio for at least one polarization [3], [4]. In order to estimate the interferometric coherence with the minimum ground contribution  $\tilde{\gamma}(\kappa_Z, \vec{w}_{\min})$ , the assumption that the coherence region of the RVoG model is a straight line along the ground-to-volume amplitude ratio  $m(\vec{w})$  is used. The 2-D coherence region is calculated, and the two extreme interferometric coherences  $\tilde{\gamma}(\kappa_Z, \vec{w}_{\max})$  and  $\tilde{\gamma}(\kappa_Z, \vec{w}_{\min})$  are estimated—associated to the polarization states  $\vec{w}_{\max}$  and  $\vec{w}_{\min}$  characterized by the maximum and minimum ground contributions—and are then used for inversion assuming  $m(\vec{w}_{\min}) = 0$ , i.e.,

$$\min_{h_v, \sigma, m, \varphi_0} \left\| \begin{bmatrix} \tilde{\gamma}(\kappa_Z, \vec{w}_{\max}) e^{-i\varphi_0} \\ \tilde{\gamma}(\kappa_Z, \vec{w}_{\min}) e^{-i\varphi_0} \end{bmatrix} - \begin{bmatrix} \tilde{\gamma}_V(\kappa_Z, h_V, \sigma, m) \\ \tilde{\gamma}_V(\kappa_Z, h_V, \sigma, m = 0) \end{bmatrix} \right\|. \quad (9)$$

The phase  $\exp(i\varphi_0)$  corresponding to the ground topography is obtained by the intersection of the line defined by  $\tilde{\gamma}(\kappa_Z, \vec{w}_{\min})$  and  $\tilde{\gamma}(\kappa_Z, \vec{w}_{\max})$  and the unit circle moving from  $\tilde{\gamma}(\kappa_Z, \vec{w}_{\min})$  to  $\tilde{\gamma}(\kappa_Z, \vec{w}_{\max})$  [1], [4], i.e.,

$$\varphi_0 = \arg \{ \tilde{\gamma}(\kappa_Z, \vec{w}_{\max}) - \tilde{\gamma}(\kappa_Z, \vec{w}_{\min})(1 - F) \} \quad (10)$$

with  $F = (-B - \sqrt{B^2 - 4AC}) / (2A)$ , coefficient  $A = |\tilde{\gamma}(\kappa_Z, \vec{w}_{\min})|^2 - 1$ , coefficient  $B = 2\text{Re}\{[\tilde{\gamma}(\kappa_Z, \vec{w}_{\max}) - \tilde{\gamma}(\kappa_Z, \vec{w}_{\min})] \tilde{\gamma}^*(\kappa_Z, \vec{w}_{\min})\}$ , and coefficient  $C = |\tilde{\gamma}(\kappa_Z, \vec{w}_{\max}) - \tilde{\gamma}(\kappa_Z, \vec{w}_{\min})|^2$ .

### C. Single-Pol Inversion

The standard DEM mode of TDX is, however, a single-pol mode operated in HH (or VV) polarization. In the case of a single-polarimetric acquisition, the parameterization of the measured interferometric coherence in terms of (4) requires four parameters: the forest height  $h_V$ , the extinction  $\sigma$ , the ground topography phase  $\varphi_0$ , and the ground-to-volume amplitude ratio  $m(\vec{w})$ . The assumption of no ground contribution, i.e., of zero ground-to-volume amplitude ratio, is not sufficient for getting a balanced inversion problem. In this case, inversion relies on additional assumptions or the availability of external information. Fixing the extinction  $\sigma$  has been proved to compromise the inversion performance as it restricts the ability of the RVoG model to interpret the spatial variability of forest structure.

The best—with respect to inversion performance—scenario is to use an external DTM to estimate the ground topographic phase  $\exp(i\varphi_0)$ . For this, the DTM is converted to phase:  $\exp(i\varphi_{DTM}) = \exp(i h_{DTM} \kappa_Z)$ . Then, the phase offset between  $\exp(i\varphi_{DTM})$  and  $\gamma(\kappa_Z, \vec{w}_i)$  is calibrated by means of a corner reflector or a bare area with sufficient high coherence  $|\tilde{\gamma}(\kappa_Z, \vec{w}_i)| > 0.98$ .  $\tilde{\gamma}(\kappa_Z, \vec{w}_i)$  can then be inverted for forest height  $h_V$  and extinction  $\sigma$  by

$$\min_{h_v, \sigma} \|\tilde{\gamma}(\kappa_Z, \vec{w}_i) \exp(-i\varphi_0) - \tilde{\gamma}_V(\kappa_Z, h_V, \sigma)\|. \quad (11)$$

For all test sites, a DTM calculated from LIDAR data was used to estimate  $\exp(i\varphi_0)$ .

## VI. INVERSION RESULTS

The two inversion scenarios were implemented and applied on all three sites. The obtained forest height maps for both cases and the reference LIDAR-derived H100 maps are shown in Fig. 18 for the Krycklan site, in Fig. 20 for the Traunstein site, and in Figs. 24 and 25 for the Mawas site.

In the single-pol case, for all test sites, in approximately 10%–15% of the samples, the inversion failed to provide a solution, probably due to a too large ground scattering contribution. Furthermore, noninvertible samples turned up in areas of low backscattering and high  $\gamma_{SNR}$ , where coherence estimates become imprecise. This mainly appeared in areas with “shadow” effects, i.e., on forest edges and on the transition from low forest to high forest areas.

In addition to the inversion problems found in the single-pol case, in the dual-pol case, the inversion performance critically depends on the difference between the phase center locations

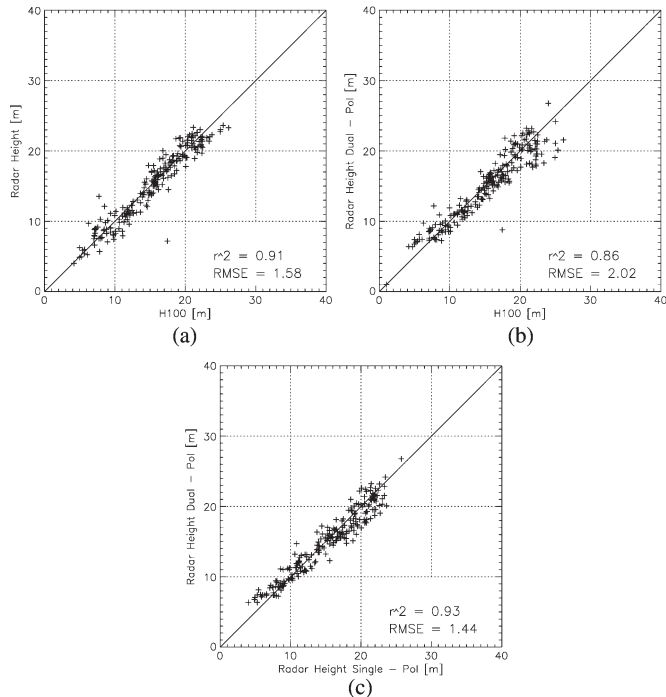


Fig. 17. Krycklan test site validation plots. (a) Single-pol inversion forest height versus LIDAR forest height. (b) Dual-pol inversion forest height versus LIDAR forest height. (c) Comparison of single-pol inversion forest height versus dual-pol inversion forest height.

in the two polarizations. In all three sites, about 20% of the samples (pixels) could not be inverted—probably because of an insufficient strong or an insufficient different ground contribution across the polarizations—making a solution of the inversion problem impossible.

Noninvertible samples were masked out and have not been considered in the cross validation.

#### A. Krycklan Test Site

1) *Single-Pol Inversion*: The low phase center height locations and the large polarimetric distances (see Figs. 6 and 12) predicted a good forest height inversion performance for the Krycklan site.

As the ground contribution in the VV channel appeared to be less than in the HH channel (see discussion in Section IV-A1), the VV channel was used for the single-baseline inversion. The validation plot for the single-pol inversion shown in Fig. 17(a) is characterized by a correlation coefficient  $r^2 = 0.91$  with a root-mean-square error RMSE = 1.58 m. One single stand was clearly underestimated (LIDAR H100 = 18 m, single-pol inversion height = 7 m)—probably affected by harvesting activities in the two years occurring between the LIDAR measurements and the TDX acquisitions. Excluding this outlier, the correlation coefficient increases to 0.93.

2) *Dual-Pol Inversion*: The validation plot for the dual-pol inversion is shown in Fig. 17(b).

Compared with the single-pol inversion, the validation for dual-pol inversion was noisier, particularly for the taller forest stands, but the overall correlation coefficient  $r^2 = 0.86$  and an RMSE of 2.02 m are convincing.

The same single stand that strongly deviated in the single-pol inversion validation also deviated here (LIDAR H100 = 18 m, dual-pol inversion height = 8 m). Again excluding this outlier, the correlation coefficient becomes 0.90.

In Fig. 17(c), the single-pol inversion forest heights were plotted against the dual-pol inversion forest heights. A correlation coefficient  $r^2 = 0.93$  in combination with an RMSE of 1.44 m underlines the consistency of the results obtained by the two approaches. In the direct comparison, the outlier stand disappeared as expected. The performance starts to degrade (in the form of an increased variance) in the region of taller forest heights in part as a consequence of the low coherence levels induced by the large vertical wavenumber ( $\kappa_Z = 0.17$ ).

The topographic variation within the scene has limited the final inversion performance due to the slope-induced modulation of the vertical wavenumber:  $\kappa_Z$  reached the maximum and minimum values for strong positive and negative slopes for which a meaningful inversion was not possible. As the forest height reaches 30 m ( $\kappa_Z = \sim 0.2$  rad/m for an HoA of 30 m),  $\kappa_Z$  values larger than 0.2 rad/m were excluded from the inversion to guarantee an unambiguous inversion. A minimum threshold for  $\kappa_Z$  was not necessary as all  $\kappa_Z$  values in the scene are larger than 0.09 rad/m (full inversion performance is granted [10]). (The Krycklan site forest height maps are presented in Fig. 18.)

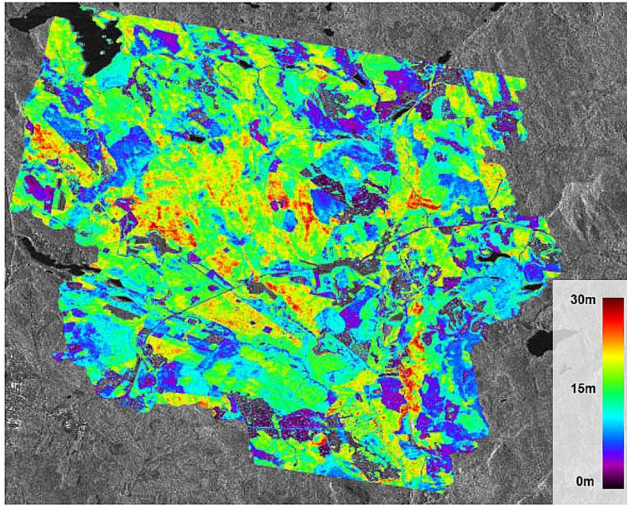
#### B. Traunstein Test Site

1) *Single-Pol Inversion*: For the Traunstein site, the single-pol inversion was applied using the HH and VV polarizations. The corresponding validation plots are shown in Fig. 19(a) for the HH polarization case and in Fig. 19(b) for the VV polarization case.

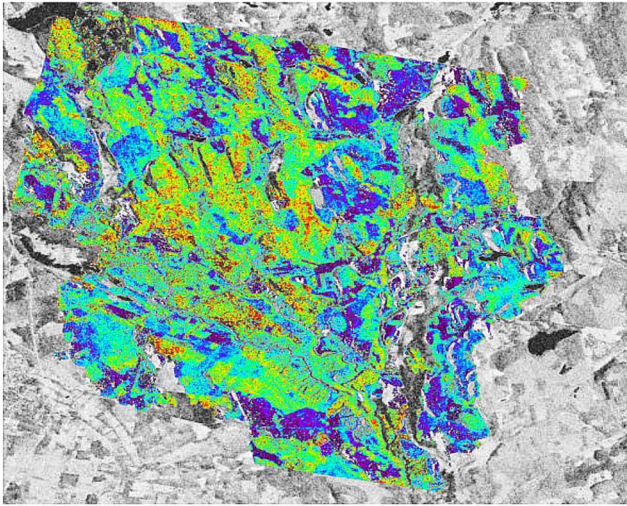
Forest heights up to 30 m have, in both cases, been accurately estimated; beyond 30 m, the performance degraded mainly because of the low coherence level. For the HH polarization, a correlation coefficient of 0.80 with an RMSE of 3.3 m has been achieved. For the VV channel, a correlation coefficient of 0.80 with an RMSE of 3.7 m has been reached. In the absence of a second appropriate TDX acquisition and in order to assess the seasonal effect on the inversion performance as the available data set was acquired in the winter in snow-covered conditions, an airborne acquisition was utilized (see Table I).

The airborne inversion performance for the VV channel is shown on the bottom left in Fig. 19(c), which is characterized by a similar performance as achieved with the TDX data (winter) set: a correlation coefficient of 0.89 with an RMSE of 2.3 m. Large stands are underestimated because the vertical wavenumber  $\kappa_Z$  is too large in some parts of the image to cover the whole height range of the prevailing forest heights (typical for airborne scenarios).

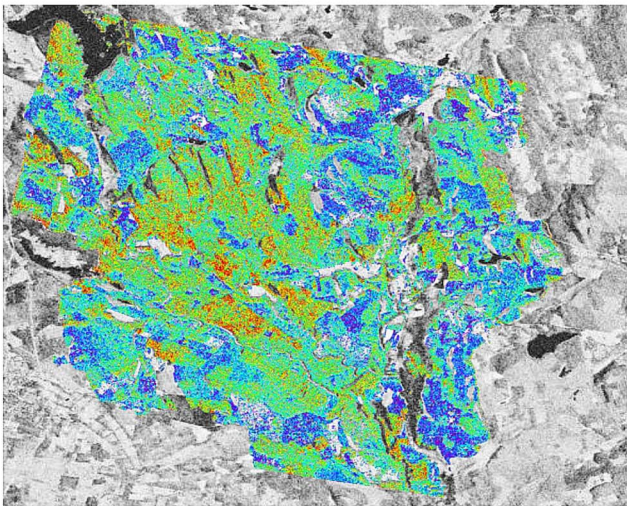
2) *Dual-Pol Inversion*: The dual-pol inversion results for Traunstein are shown in the plot in Fig. 19(d). The correlation of the LIDAR with the dual-pol inversion results is noisier ( $r^2 = 0.77$ ). The RMSE is 2.8 m, clearly lower than for the single-pol inversion. Similar to the single-pol case, the inversion performance degrades for stands larger than 30 m. (The Traunstein test site forest height maps are presented in Fig. 20.)



(a)



(b)



(c)

Fig. 18. Krycklan test site forest height maps. (a) LIDAR H100 superimposed on radar amplitude image. (b) Single-pol inversion forest heights (VV) superimposed on interferometric coherence scaled from 0 (black) to 1 (white). (c) Dual-pol inversion forest heights superimposed on interferometric coherence scaled from 0 (black) to 1 (white).

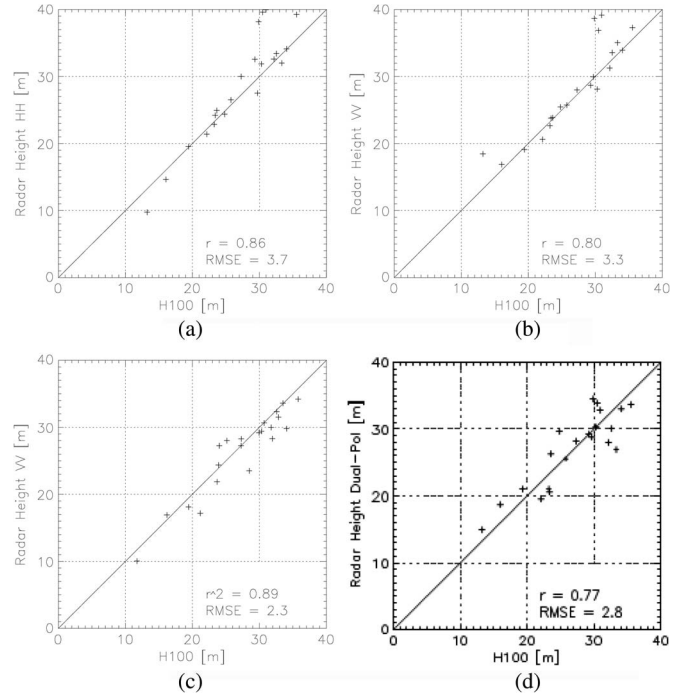


Fig. 19. Traunstein test site validation plots. (a) TDX single-pol inversion forest height HH polarization versus LIDAR forest height. (b) TDX single-pol inversion VV polarization versus LIDAR forest height. (c) E-SAR airborne single-pol inversion forest height VV polarization versus LIDAR forest height. (d) TDX dual-pol inversion forest height versus LIDAR forest height.

### C. Mawas Test Site

1) *Single-Pol Inversion*: The single-pol inversion was applied on all four available Mawas acquisitions using the HH and VV polarizations. The corresponding validation plots are shown in Figs. 21 and 22 (riverine forest = blue dots, peat swamp forest = red dots). As already indicated by the phase center height plots, no significant differences between the HH and VV polarization were expected.

The acquisition in the dry season (August 25) clearly underestimated the forest height with an RMSE of 3.3 m. This was probably caused by the insufficiency of the inversion model to fit the actual situation. At the end of the dry season, tree tops are dried out, and the leaves have sometimes fallen off. The open canopy consisting of single trees with dried out tree tops and partially bare branches at the end of the dry season could have caused scattering from the tree crowns to be less pronounced and could have violated the assumption of an exponential backscatter function as used in the inversion model; in addition, the presence of a ground scattering contribution in all polarizations available cannot be excluded, particularly in the dry season.

With the beginning of the rainy season, forest height estimates are clearly improved and reach RMSE levels down to 2.2 m for the HH channel and 1.9 m for the VV channel. The correlation coefficients are, for all acquisitions, very high, with values between 0.97 and 0.98.

2) *Dual-Pol Inversion*: The validation plots for all four acquisition dates are shown in Fig. 23.

The two forest types, i.e., the riverine forest (blue dots in Fig. 23) and the peat swamp forest (red dots in Fig. 23), has

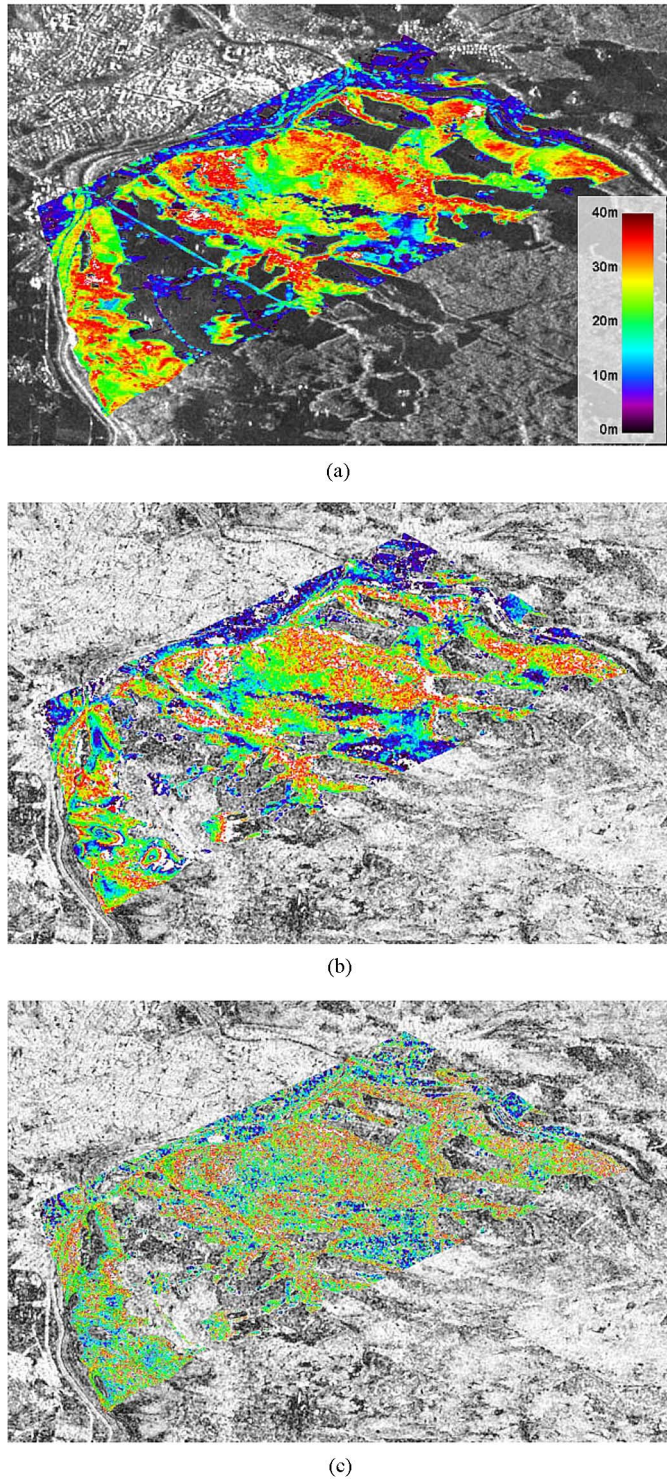


Fig. 20. Traunstein test site forest height maps. (a) LIDAR H100 superimposed on radar amplitude image. (b) Single-pol inversion forest heights (VV) superimposed on interferometric coherence scaled from 0 (black) to 1 (white). (c) Dual-pol inversion forest heights superimposed on interferometric coherence scaled from 0 (black) to 1 (white).

each shown different behaviors: The estimates of the riverine forest are approximately 5 m higher than the estimates of the peat swamp forest.

The dual-pol inversion performed worse compared with the single-pol inversion for the Mawas site. Even in the dry

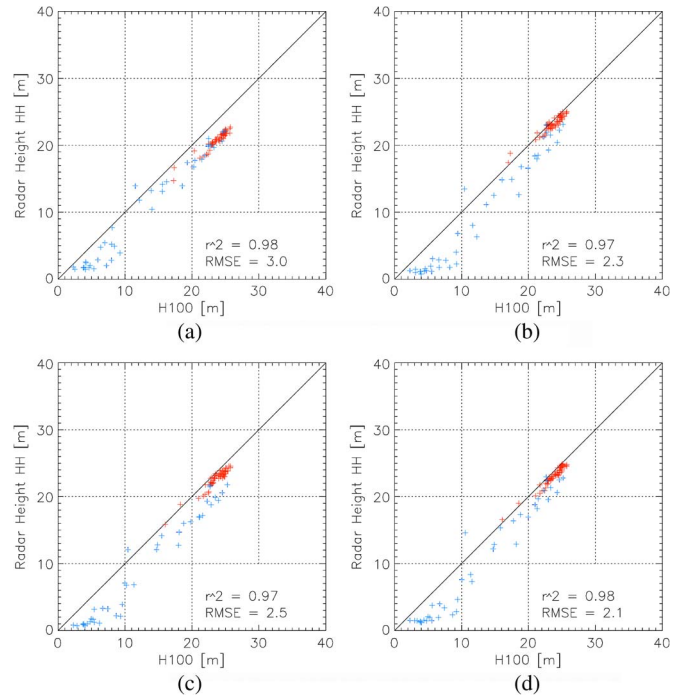


Fig. 21. Mawas test site validation plots: single-pol inversion forest height versus LIDAR forest height in HH polarization. (a) August 25, 2011. (b) December 13, 2011. (c) December 24, 2011. (d) January 4, 2012. (Blue dots) Riverine forest. (Red dots) Peat swamp forest.

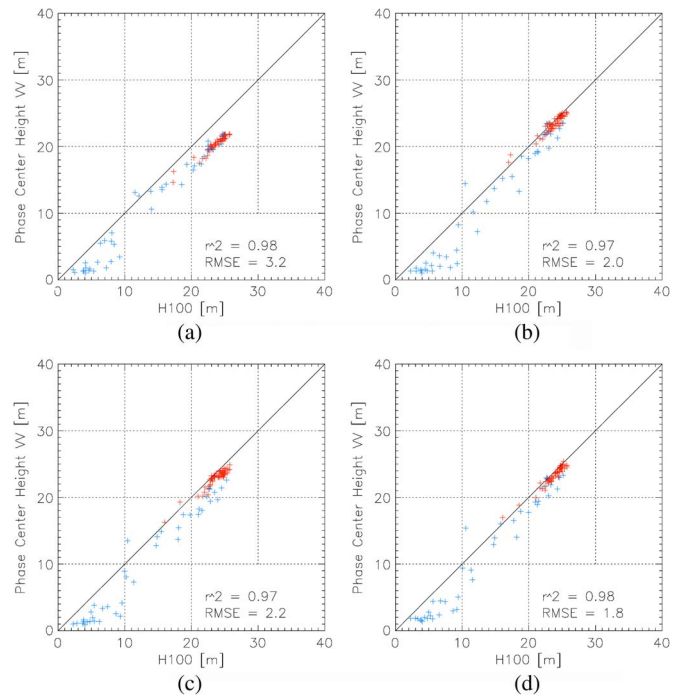


Fig. 22. Mawas test site validation plots: single-pol inversion forest height versus LIDAR forest height in VV polarization. (a) August 25, 2011. (b) December 13, 2011. (c) December 24, 2011. (d) January 4, 2012. (Blue dots) Riverine forest. (Red dots) Peat swamp forest.

season acquisition (August 25, 2011), low forests heights were overestimated, but tall forests stands (the peat swamp forest) were underestimated. With the beginning of the rainy season, all estimates increase by 4 m–5 m. Now, all riverine forest stands

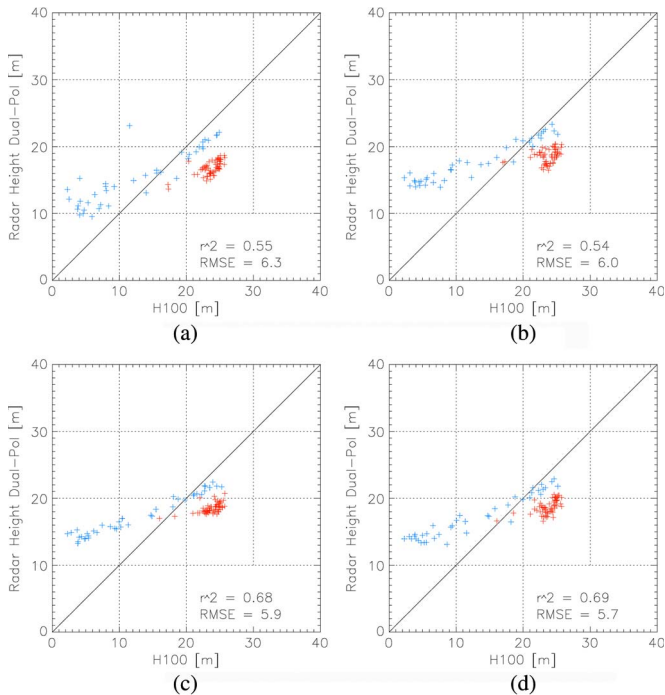


Fig. 23. Mawas test site validation plots: dual-pol inversion. (a) August 25, 2011. (b) December 13, 2011. (c) December 24, 2011. (d) January 4, 2012. (Blue dots) Riverine forest. (Red dots) Peat swamp forest.

were overestimated, and the peat swamp forest stands were still underestimated.

There were no significant improvements of the result for the last two acquisitions of the rainy season. The poor performance is caused by two reasons: The overestimation of the lower height ranges of the riverine forest is primarily induced by the small vertical wavenumber that is insufficient to compensate the impact of residual nonvolumetric decorrelation contributions [10]. With increasing forest height, the impact of the residual nonvolumetric decorrelation contributions becomes smaller, and the estimates of the taller riverine forest stands are unbiased. This error source may be compensated by using larger spatial baselines (i.e., larger vertical wavenumbers). Indeed, the overestimation is stronger in the rainy season acquisitions acquired with a vertical wavenumber of 0.07 rad/m and weaker for the dry season acquisition acquired with a slightly larger vertical wavenumber of 0.12 rad/m. In the Krycklan site, the large(r) vertical wavenumber of 0.17 rad/m allows the unbiased estimation of low forest heights, as shown in Fig. 17.

The underestimation of the peat-swamp forest is more difficult to interpret. It was probably induced by the used inversion model, which failed to reflect the right vertical scattering distribution.

The single emergent tree over a less dense canopy with extensive undergrowth violates the assumption of an exponential backscatter function with zero ground and leads to an underestimation of height [37]. Note that both errors were, by far, less important in the single-pol inversion (comparison with Figs. 21 and 22). The ground location information implied by the use of the external DEM allowed for the compensation of a wide range of estimation biases. (The Mawas site forest height maps are presented in Figs. 24 and 25.)

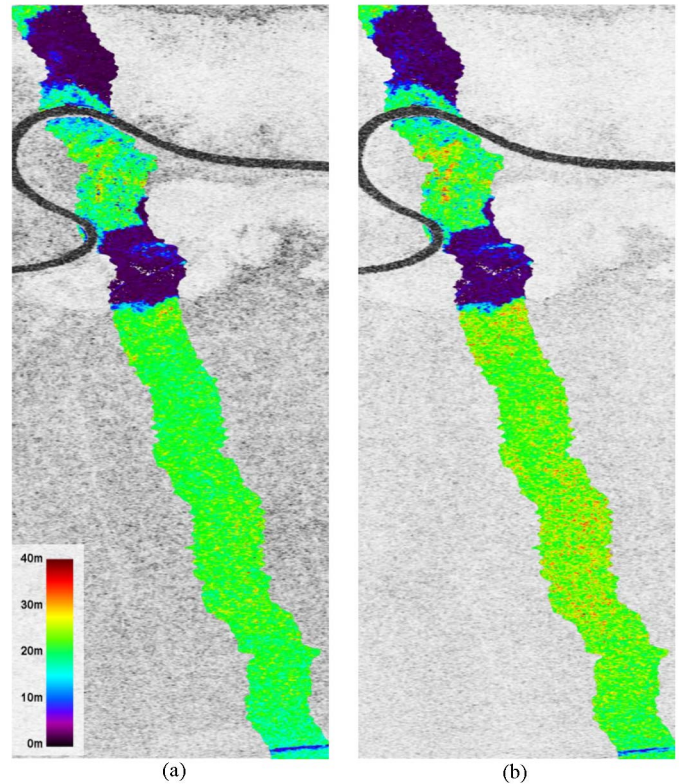


Fig. 24. Mawas test site forest heights maps (bottom: near range, top: far range). (a) Interferometric coherence scaled from 0 (black) to 1 (white) superimposed by single-pol inversion forest heights in HH polarization from the acquisition of August 25, 2011. (b) Interferometric coherence scaled from (black) 0 to (white) 1 superimposed by single-pol inversion forest heights in VV polarization from the acquisition of January 4, 2012.

## VII. CONCLUSION

In this paper, the potential of TDX Pol-InSAR data for quantitative forest parameter estimation has been investigated. For this, a large number of single- and dual-pol TDX data sets acquired over three different forest sites—a boreal, a temperate, and a tropical site—at different acquisition modes have been analyzed.

The suitability of TDX for Pol-InSAR forest applications depends on the penetration capability of X-band into forest vegetation and on the polarimetric diversity of the interferometric coherence. Both effects were evaluated over all three sites for different acquisition geometries (i.e., on the incidence angle and spatial baseline) and for different environmental and seasonal conditions.

For all sites, a strong correlation between the (height of the) phase center location and forest (top) height could be established. The corresponding correlation coefficients reached values of 0.9 and higher. The correlation varies with seasonal and environmental changes. Clear seasonal dependence could be observed between summer and winter acquisitions at the European test sites. For the tropical site, the difference between wet and dry seasons was weaker.

For the Krycklan site, acquisitions at different look angles ( $19^\circ$  and  $32^\circ$ ) were analyzed, indicating only a weak effect of the incidence angle on the penetration. For the Traunstein site, impact of incidence (look) angle appeared stronger than at the Krycklan site. However, here, differences in phase center

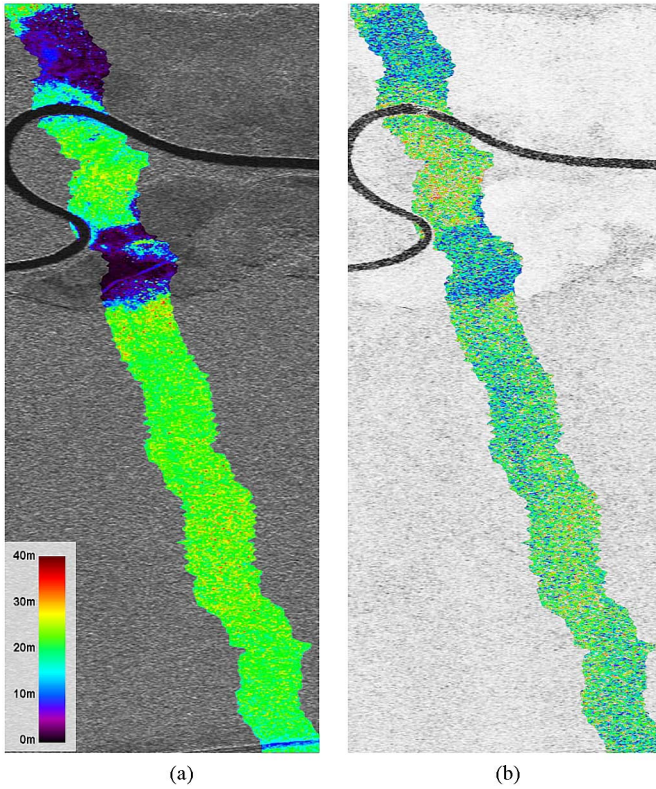


Fig. 25. Mawas test site forest heights maps (bottom: near range, top: far range). (a) Radar amplitude image in HH polarization superimposed by LIDAR H100. (b) Interferometric coherence scaled from 0 (black) to 1 (white) superimposed by dual-pol forest heights from the acquisition of January 4, 2012.

height due to different incidence (look) angles are mixed up with seasonal effects.

The synthesis of the results suggests an unexpected high penetration at X-band but leaves open the question of whether the penetration is induced by the propagation through the vegetation volume or partially through gaps in the vegetation layer that become relevant at the spatial resolution of the TDX data [38].

The polarimetric dependence of the interferometric coherence (expressed by means of the length of the dual-pol coherence region) was strongly correlated to forest height in all sites. At the same time, the effect of seasonal and environmental variability was clearly visible: For the boreal site, the penetration during the winter can be interpreted only with a sufficient large ground scattering contribution that makes an inversion based on the assumption of a “zero ground component” suboptimal.

The summer acquisitions were characterized by a smaller ground contribution supporting “zero ground component” inversion schemes. For the temperate site, the winter acquisitions seemed to be better suited for inversion than the summer acquisitions as penetration was higher and the whole volume is “seen” by the radar (due to the lower attenuation in winter). In the tropical case, the impact of seasonal effects on the polarimetric diversity was rather small. This allows concluding that seasonal adapted acquisitions could improve the inversion performance and probably increase the number of forest types that can be investigated by means of Pol-InSAR techniques at X-band.

Based on these observations, two forest height estimation approaches—one for the single-pol case based on the avail-

ability of an external DTM and one for the dual-pol case that does not require any *a priori* knowledge—have been proposed, implemented, and applied on the available data sets. The obtained height estimates have been cross validated against LIDAR reference measurements.

In forest conditions that allow a sufficient penetration at X-band, the performance of the two approaches was comparable and surprisingly high, with a correlation of  $r^2 = 0.86$  in the boreal site and  $r^2 = 0.77$  in the temperate site for the dual-pol case. At denser conditions, the variance of the dual-pol estimates increased ( $r^2 = \sim 0.50$  in the tropical site) and finally saturated with increasing height due to the insufficient penetration. Note that the single-pol inversion was not affected by saturation as it does not require a penetration until the ground.

The choice of spatial baseline (expressed in terms of the vertical wavenumber) has a critical impact on the inversion performance. Too small spatial baselines limit the sensitivity to forest height variation and/or increase the errors induced by uncompensated nonvolumetric decorrelation contributions [10]. Too large baselines lead to (too) low coherence levels and limit the range of heights that can be mapped. The fact that TDX (as discussed in Section II-B) follows predefined vertical wavenumber cycles that are optimized with respect to the DEM acquisition strategy restricts the availability of optimum vertical wavenumber regimes for forest parameter estimation. However, the selection of a more appropriate beam (i.e., look angle) provides one degree of freedom to partially optimize the given spatial baseline configuration.

Regarding now the choice of polarization, the TDX and TSX instruments allow the acquisition not only of conventional cross-polarized dual-pol data (i.e., HH and VH or VV and HV) but also copolarized dual-pol data (i.e., HH and VV). The relative small ground scattering contributions at X-band compared with the high additive noise level at the cross-polarized channels (with a noise equivalent sigma zero NESZ on the order of 20–24 dB; see Fig. 15) make the copolarized dual-pol mode better suited (in terms of performance) for Pol-InSAR applications [34], [39].

The availability of quad-pol acquisitions—acquired in a later dedicated quad-pol operation phase—can improve the performance in terms of variance and reduce the number of samples with nonvalid solutions. However, the constraints imposed by the penetration depth and the low NESZ will remain. Finally, the inversion of multiple acquisitions acquired with different spatial baselines may be an alternative way to improve inversion performance. In this case, in addition to the inherent limitation of penetration into dense(r) forest conditions, the variability of the forest structure in the time between the acquisitions has to be accounted. An exception is the alternating bistatic mode, but this mode is limited to two baselines in a single polarization.

Finally, the achieved performance clearly indicates the advantage of a spaceborne single-pass interferometric implementation for forest applications. The absence of temporal decorrelation allows the achievement of a new quality in measurement accuracy that may allow the development of new applications and make systematic monitoring of forest structure parameters—preferably at a lower frequency band—possible.

## ACKNOWLEDGMENT

The authors would like to thank the TDX team for the fast access to the data and C. Wecklich for his valuable comments to improve the quality of this paper. They would also like to thank P. Prats for his support in data processing issues and V. Böhm from KALTENG Consultants for providing the LIDAR data over Mawas.

## REFERENCES

- [1] S. R. Cloude, *Polarisation Applications in Remote Sensing*. London, U.K.: Oxford Univ. Press, 2010.
- [2] S. R. Cloude and K. P. Papathanassiou, "Polarimetric SAR interferometry," *IEEE Trans. Geosci. Remote Sens.*, vol. 36, no. 5, pp. 1551–1565, Sep. 1998.
- [3] K. P. Papathanassiou and S. R. Cloude, "Single-baseline polarimetric SAR interferometry," *IEEE Trans. Geosci. Remote Sens.*, vol. 39, no. 11, pp. 2352–2363, Nov. 2001.
- [4] R. N. Treuhaft, S. N. Madsen, M. Moghaddam, and J. J. van Zyl, "Vegetation characteristics and underlying topography from interferometric data," *Radio Sci.*, vol. 31, no. 6, pp. 1449–1495, Nov./Dec. 1996.
- [5] I. Hajnsek, F. Kugler, S. Lee, and K. Papathanassiou, "Tropical forest parameter estimation by means of Pol-InSAR: The INDREX II campaign," *IEEE Trans. Geosci. Remote Sens.*, vol. 47, no. 2, pp. 481–493, Feb. 2009.
- [6] J. Praks, F. Kugler, K. P. Papathanassiou, I. Hajnsek, and M. Hallikainen, "Tree height estimation for boreal forest by means of L and X band PolInSAR and HUTSCAT scatterometer," *IEEE Trans. Geosci. Remote Sens. Lett.*, vol. 4, no. 3, pp. 466–470, Jul. 2007.
- [7] F. Garestier, P. C. Dubois-Fernandez, and K. P. Papathanassiou, "Pine forest height inversion using single-pass X-band PolInSAR data," *IEEE Trans. Geosci. Remote Sens.*, vol. 46, no. 1, pp. 56–68, Jan. 2008.
- [8] J. Praks, O. Antropov, and M. T. Hallikainen, "LIDAR-aided SAR interferometry studies in boreal forest: Scattering phase center and extinction coefficient at X- and L-band," *IEEE Trans. Geosci. Remote Sens.*, vol. 50, no. 10, pp. 3831–3843, Oct. 2012.
- [9] K. P. Papathanassiou and S. R. Cloude, "The effect of temporal decorrelation on the inversion of forest parameters from Pol-InSAR data," in *Proc. IGARSS*, Toulouse, France, 2003, pp. 1429–1431, [CD-ROM].
- [10] S.-K. Lee, F. Kugler, K. Papathanassiou, and I. Hajnsek, "Quantification of temporal decorrelation effects at L-band for polarimetric SAR interferometry applications," *IEEE J. Sel. Top. Appl. Earth Obs. Remote Sens.*, vol. 6, no. 3, pp. 1351–1367, Jun. 2013.
- [11] M. Lavalley, M. Simard, and S. Hensely, "A temporal decorrelation model for polarimetric radar interferometers," *IEEE Trans. Geosci. Remote Sens.*, vol. 50, no. 7, pp. 2880–2888, Jul. 2012.
- [12] F. Kugler, S. Sauer, S.-K. Lee, K. Papathanassiou, and I. Hajnsek, "Potential of TanDEM-X for forest parameter estimation," in *Proc. EUSAR*, Aachen, Germany, 2010, pp. 1–4.
- [13] S. Solberg, R. Astrup, T. Gobakken, E. Nsset, and D. J. Weydahl, "Estimating spruce and pine biomass with interferometric X-band SAR," *Remote Sens. Environ.*, vol. 114, no. 10, pp. 2353–2360, Oct. 15, 2010.
- [14] R. Perko, H. Raggam, J. Deutscher, K. Gutjahr, and M. Schardt, "Forest assessment using high resolution SAR data in x-band," *Remote Sens.*, vol. 3, no. 4, pp. 792–815, Apr. 2011.
- [15] M. Nilsson and J. Holmgren, "Prediction of forest variables using LiDAR measurements with different footprint sizes and measurement densities," in *Proc. ScandLaser Sci. Workshop Airborne Laser Scanning Forests*, Umeå, Sweden, Sep. 3–4, 2003, pp. 125–133.
- [16] Izzawati, E. D. Wallington, and I. H. Woodhouse, "Forest height retrieval from commercial X-band SAR products," *IEEE Trans. Geosci. Remote Sens.*, vol. 44, no. 4, pp. 863–870, Apr. 2006.
- [17] I. H. Woodhouse and E. D. Izzawati, "Edge effects on tree height retrieval using X-band interferometry," *IEEE Geosci. Remote Sens. Lett.*, vol. 3, no. 3, pp. 344–348, Jul. 2006.
- [18] D. H. Hoekman and C. Verekamp, "Observation of tropical rain forest trees by airborne high-resolution radar," *IEEE Trans. Geosci. Remote Sens.*, vol. 39, no. 3, pp. 584–594, Mar. 2001.
- [19] C. Verekamp and D. H. Hoekman, "High-resolution InSAR image simulation for forest canopies," *IEEE Trans. Geosci. Remote Sens.*, vol. 40, no. 7, pp. 1648–1655, Jul. 2002.
- [20] G. Krieger, A. Moreira, H. Fiedler, I. Hajnsek, M. Werner, M. Younis, and M. Zink, "TanDEM-X: A satellite formation for high-resolution SAR interferometry," *IEEE Trans. Geosci. Remote Sens.*, vol. 45, no. 11, pp. 3317–3341, Nov. 2007.
- [21] G. Krieger, M. Zink, M. Bachmann, B. Bräutigam, D. Schulze, M. Martone, P. Rizzoli, U. Steinbrecher, J. W. Antony, F. De Zan, I. Hajnsek, K. Papathanassiou, F. Kugler, M. Rodriguez Cassola, M. Younis, S. Baumgartner, P. López-Dekker, P. Prats, and A. Moreira, "TanDEM-X: A radar interferometer with two formation-flying satellites," *Acta Astron.*, vol. 89, pp. 83–98, Aug./Sep. 2013.
- [22] "TerraSAR-X ground segment basic product specification document," DLR, Oberpfaffenhofen, Germany, TX-GS-DD-3302, Issue: 1.6, Mar. 18, 2009. [Online]. Available: [https://tandemx-science.dlr.de/TX-GS-DD-3302\\_Basic-Products-Specification-Document\\_V1.6.pdf](https://tandemx-science.dlr.de/TX-GS-DD-3302_Basic-Products-Specification-Document_V1.6.pdf)
- [23] M. Bachmann, D. Schulze, C. Ortega-Miguez, D. Polimeni, J. Böer, J. Hueso Gonzalez, J. Walter Antony, G. Krieger, B. Bräutigam, M. Schwerdt, and M. Zink, "Acquisition status and calibration of the interferometric system," in *Proc. IGARSS*, Munich, Germany, Jul. 2012, pp. 1900–1903.
- [24] H. Fiedler and G. Krieger, "Close formation of passive receiving micro-satellites," in *Proc. 18th Int. Symp. Space Flight Dyn.*, Munich, Germany, 2004, pp. 47–52.
- [25] A. van Laar and A. Akca, *Forest Mensuration (Managing Forest Ecosystems)*. Dordrecht, The Netherlands: Springer-Verlag, 2007, pp. 118–121.
- [26] M. Heurich, T. Schneider, and E. Kennel, "Laser scanning for identification of forest structures in the Bavarian Forest National Park," in *Proc. ScandLaser Sci. Workshop Airborne Laser Scanning Forests*, Umeå, Sep. 3–4, 2003, pp. 125–133.
- [27] T. Aulinger, T. Mette, K. P. Papathanassiou, I. Hajnsek, M. Heurich, and P. Krzystek, "Validation of heights from interferometric SAR and LIDAR over the temperate Forest Site National Park Bayerischer Wald," in *Proc. 2nd Int. Workshop POLinSAR*, Frascati, Italy, Jan. 17–21, 2005, pp. 1–6, [CD-ROM].
- [28] E. Assmann and F. Franz, *Vorläufige Fichten-Ertragstafel für Bayern*. München, Germany: Institut für Ertragskunde der Forstl. Forschungsanst, 1963, 104 S.
- [29] R. Horn, "The DLR airborne SAR project E-SAR," in *Proc. IEEE Trans. Geosci. Remote Sens. Symp.*, Lincoln, NE, USA, May 1996, vol. 3, pp. 1624–1628.
- [30] A. Reigber, R. Horn, A. Nottensteiner, P. Prats, R. Scheiber, K. H. Bethke, and S. Baumgartner, "Current status of DLR's new F-SAR sensor," in *Proc. EUSAR*, Aachen, Germany, Jun. 7–10, 2010, pp. 1078–1081, VDE Verlag GmbH.
- [31] H.-D. V. Böhm, V. Liesenberg, and S. H. Limin, "Multi-temporal airborne LiDAR-survey and field measurements of tropical peat swamp forest to monitor changes," *IEEE J. Sel. Top. Appl. Earth Obs. Eemote Sens.*, vol. 6, no. 3, pp. 1524–1530, Jun. 2013.
- [32] S. R. Cloude and K. P. Papathanassiou, "Three-stage inversion process for polarimetric SAR interferometry," *Proc. Inst. Elect. Eng.—Radar Sonar Navigat.*, vol. 150, no. 3, pp. 125–134, Jun. 2003.
- [33] D. Just and R. Bamler, "Phase statistics of interferograms with applications to synthetic aperture radar," *Appl. Opt.*, vol. 33, no. 20, pp. 4361–4368, Jul. 1994.
- [34] S. Cloude, "An assessment of the PolInSAR performance of TanDEM-X for forestry applications," in *Proc. PolInSAR*, Frascati, Italy, Jan. 24–28, 2011, pp. 1–9.
- [35] R. N. Treuhaft and P. Siquiera, "Vertical structure of vegetated land surfaces from interferometric and polarimetric radar," *Radio Sci.*, vol. 36, no. 1, pp. 141–177, Jan./Feb. 2000.
- [36] F. Gatelli, A. Monti Guamieri, F. Parizzi, P. Pasquali, C. Prati, and F. Rocca, "The wavenumber shift in SAR interferometry," *IEEE Trans. Geosci. Remote Sens.*, vol. 32, no. 4, pp. 855–865, Jul. 1994.
- [37] F. Kugler, S.-K. Lee, and K. Papathanassiou, "Estimation of forest vertical structure parameter by means of multi baseline Pol-InSAR," in *Proc. IGARSS*, Cape Town, South Africa, Jul. 2009, pp. IV-721–IV-724.
- [38] F. De Zan, G. Krieger, and P. López-Dekker, "On some spectral properties of TanDEM-X interferograms over forested areas," *IEEE Geosci. Remote Sens. Lett.*, vol. 10, no. 1, pp. 71–75, Jan. 2013.
- [39] F. Kugler, I. Hajnsek, and K. Papathanassiou, "Forest parameter characterisation by means of TerraSAR-X and TanDEM-X (polarimetric and) interferometric data," in *Proc. PolInSAR*, Vancouver, BC, USA, Jan. 24–29, 2011, pp. 2578–2581.



**Florian Kugler** was born in Bavaria, Germany, in 1974. He received the Dipl.Ing. degree in forestry science from Technische Universität München, Freising, Germany, in 2004. He is currently working toward the Ph.D. degree at the German Aerospace Center (DLR), Oberpfaffenhofen, Germany.

Since October 2008, he has been also a Research Scientist with DLR. His research focuses on remote sensing on forests, by using polarimetric synthetic aperture radar interferometry.



**Daniel Schulze** was born in Germany in 1975. He received the Diploma degree in aerospace technology from the Technical University of Berlin, Berlin, Germany, in 2002.

Since 2004, he has been with the Satellite SAR System Department, Microwaves and Radar Institute, German Aerospace Center (DLR), Oberpfaffenhofen, Germany. He worked for the TerraSAR-X synthetic aperture radar (SAR) satellite project within the System Engineering and Calibration (SEC) Segment of Ground Segment. In the years 2004 and 2005, he implemented the Instrument Command Generator and supervised the Long Term Database implementation for Instrument Operations and Calibration Segment, which are the operational systems of SEC. From 2005 to 2008, he was a System Engineer for the SEC Segment. The SEC is in charge of all SAR relevant system engineering aspects and the SAR instrument operation and calibration. It is the interfaces between all SAR relevant parts of the space segment and the ground segment and thus includes the review of the space segment design and performance measurements. During his work as a System Engineer, the foundation for the successful TerraSAR-X commissioning and operational phase was laid. Since 2007, he has been working for the follow-on mission TanDEM-X. He became the Project Manager of the joined TerraSAR-X and TanDEM-X SEC Segment in 2008. Both SAR satellite missions exceeded their expectations regarding image performance and reliability. Apart from the work in the TerraSAR-X/TanDEM-X context, he was a Consultant for SAR-related topics of the DLR's Satellite SAR System Department involvement in the Spanish SAR satellite mission PAZ.



**Irena Hajnsek** (AM'01–M'06–SM'09–F'13) received the Dipl. degree (with honors) from the Free University of Berlin, Berlin, Germany, in 1996 and the Dr. degree (with honors) from the Friedrich Schiller University of Jena, Jena, Germany, in 2001.

From 1996 to 1999, she was with the Microwaves and Radar Institute, German Aerospace Center (DLR-HR), Oberpfaffenhofen, Germany. From 1999 to 2000, she was with the Institut d'Electronique et de Télécommunications de Rennes, University of Rennes 1, Rennes, France, for ten months and with Applied Electromagnetics, St. Andrews, Scotland, for four months, in the frame of the European Training and Mobility for Young Researchers Program Radar Polarimetry Network. In 2005, she was a Guest Scientists with the University of Adelaide, Adelaide, Australia, for six weeks. She was the science Coordinator of the German satellite mission TanDEM-X. From 2009 to 2013, she was a member of the ESA Mission Advisory Group of the 7th Explorer Mission CoReH2O. Since November 2009, she has been a Professor of earth observation with the Institute of Environmental Engineering, Swiss Federal Institute of Technology (ETH) Zürich, Zurich, Switzerland, and the Head of the Polarimetric SAR Interferometry Research Group with DLR-HR. Her main research interests are in electromagnetic propagation and scattering theory, radar polarimetry, SAR and interferometric SAR data processing techniques, and environmental parameter modeling and estimation.

Dr. Hajnsek has been a member of the IEEE Geoscience and Remote Sensing Society AdCom since 2013 and was a Technical Program Cochair of the IEEE International Geoscience and Remote Sensing Symposium 2012 in Munich.



**Hans Pretzsch** was born in Düsseldorf, Germany, in 1957. He received the Ph.D. degree in forest growth and yield science and biometrics from Ludwig-Maximilians-Universität München, München, Germany, in 1985, the Prof. h.c. degree from the Czech University of Life Sciences in Prague, Prague, Czech Republic, in 2001, and the Dr. h.c. degree from the Czech University of Agriculture of Prague, Prague, in 2008.

Since 1994, he has been a Professor of forest growth and yield science with Technische Universität München, München, where he is responsible for the network of long-term experimental plots in Bavaria, which date back to 1860, and for the management of the municipal forest enterprise Traunstein/Bavaria. He currently teaches forestry and sustainable resource management to undergraduate and graduate students, as well as professional foresters. He has authored/coauthored over 100 publications in international journals, conferences, and workshops. For the past 20 years, he has focused his research on general rules of tree and stand growth, forest modeling, mixed stand analysis, structural allometry under competitive stress, diagnosis of forest growth disturbances, and applications of terrestrial LiDAR and computer tomography for analysis of structures on tree and stand level.

Dr. Pretzsch is an Editor of the *European Journal of Forest Research*. He was a recipient of the Biometric Research Award from the Biometrical Society, the Danzer Research Award from the Danzer Group, and the W. L. Pfeil Award from Toepfer Stiftung F.V.S.



**Konstantinos P. Papathanassiou** (AM'01–M'06–SM'09–F'13) received the Dipl.Ing degree (with honors) and the Dr. degree (with honors) from the Technical University of Graz, Graz, Austria, in 1994 and 1999, respectively.

From 1992 to 1994, he was with the Institute for Digital Image Processing (DIBAG), Joanneum Research, Graz. Between 1995 and 1999, he was with the Microwaves and Radar Institute, German Aerospace Center (DLR-HR), Oberpfaffenhofen, Germany. From 1999 to 2000, he was a European Union Postdoctoral Fellow with Applied Electromagnetics, St. Andrews, Scotland. Since October 2000, he has been a Senior Scientist with DLR-HR, leading the Information Retrieval Research Group. He has authored/coauthored over 100 publications in international journals, conferences, and workshops. His main research interests are in polarimetric and interferometric processing and calibration techniques, polarimetric SAR interferometry, and the quantitative parameter estimation from SAR data, as well as in SAR mission design and SAR mission performance analysis.

Dr. Papathanassiou was the recipient of the IEEE GRSS IGARSS Symposium Prize Paper Award in 1998, the Best Paper Award of the European SAR Conference in 2002, the DLR Science Award in 2002, and the DLR Senior Scientist Award in 2011.